

## Response to Comments from Anonymous Referee #1

Comments to the Author (General comments): In this paper, the impact of dust chemistry on regional air quality is studied deeply from a super dust storm on March 2010, especially the differences of the two paths. What's more, this study also highlight that the dust also can enhance the heterogeneous reactions, resulting high pollutions, different from the previous study that the dust has a clean effect on the local pollutants. I'm interesting to see this paper published before revised as below suggestion.

We greatly thank the reviewer for his/her careful reading of our manuscript and the supportive comments. We address the referee's specific comments as below. Please check the highlighted sentences in the revised manuscript for those changes.

### Specific comments:

1. Line 20, please reconfirm the dust storm date of "March 19-27" is right. I think it should be "March 19-23".

Thanks for pointing out this typo. The dust storm date is from March 19-23 and it is corrected in the revised version as "Near surface and vertical in situ measurements of atmospheric particles were conducted in Shanghai during March 19-23, 2010 to explore the transport and chemical evolution of dust particles in a super dust storm."

2. Line 124, same to the question above.

The dust storm date is from March 19-23, but the TSP samples in this study were collected from March 19-27, including the dust days and the non-dust days after the dust episodes. Thus, the date in Line 124 is correct.

3. Line 163. How get the  $C_{high}$  and  $C_{low}$  to calculate the  $C$ ? It seems that you can derive the  $I_{high}$  and  $I_{low}$  from the API grading limited value table according your description. Can you derive the  $i_{high}$  and  $I_{low}$  directly from the table?

Thanks for the comments. In China, six grades of air pollution of excellent, good, slightly polluted, lightly polluted, moderately polluted, and heavily polluted were set corresponding to the API scales of 0-50, 51-100, 101-150, 151-200, 201-300, and >300, respectively. Both API values of 50, 100, 200, 300, 400, and 500 and their corresponding concentrations of air pollutants were defined in the API grading limited value table as shown in Table S1. According to the definition of API in China, the API value of air pollutants was calculated as  $I = (I_{high} - I_{low})(C - C_{low}) / (C_{high} - C_{low}) + I_{low}$ , where  $C$  and  $I$  are the concentration and the API value of a specific air pollutant, respectively.  $I_{high}$  and  $I_{low}$  stand for the two values in the API grading limited value table that mostly approach to value  $I$ , respectively.  $C_{high}$  and  $C_{low}$  represent the concentrations corresponding to  $I_{high}$  and  $I_{low}$ , respectively. Thus, once getting the API

value of  $PM_{10}$ , it can be converted to  $PM_{10}$  concentration as  $C = (I - I_{low})(C_{high} - C_{low}) / (I_{high} - I_{low}) + C_{low}$ .

Table S1. The API grading limited value and the corresponding concentrations of air pollutants in China (Ministry of Environmental Protection of the People's Republic of China, Technical requirements for urban ambient air quality daily report and forecast, 2008, [http://www.zhb.gov.cn/gkml/hbb/bgth/200910/t20091022\\_174917.htm](http://www.zhb.gov.cn/gkml/hbb/bgth/200910/t20091022_174917.htm)).

API	Concentration ( $\mu\text{g}/\text{m}^3$ ) *				
	SO <sub>2</sub>	NO <sub>2</sub>	PM <sub>10</sub>	CO	O <sub>3</sub>
50	50	80	50	5000	120
100	150	120	150	10000	200
200	800	280	350	60000	400
300	1600	565	420	90000	800
400	2100	750	500	120000	1000
500	2620	940	600	150000	1200

\*24h average concentrations for SO<sub>2</sub>, NO<sub>2</sub>, PM<sub>10</sub>, and CO and 8h average concentrations for O<sub>3</sub>

We have revised Section 2.3 as below.

Air pollution index (API) data in 86 major cities (locations shown in Fig. 1a) over China were obtained from the data center of Ministry of Environmental Protection of China (<http://datacenter.mep.gov.cn/>). In China, six grades of air pollution of excellent, good, slightly polluted, lightly polluted, moderately polluted, and heavily polluted were set corresponding to the API scales of 0-50, 51-100, 101-150, 151-200, 201-300, and >300, respectively. Both API values of 50, 100, 200, 300, 400, and 500 and their corresponding concentrations of air pollutants were defined in the API grading limited value table as shown in Table S1. According to the definition of API in China, the API value of air pollutants is calculated as  $I_x = (I_{x, high} - I_{x, low})(C_x - C_{x, low}) / (C_{x, high} - C_{x, low}) + I_{x, low}$ , where  $C_x$  and  $I_x$  are the concentration and the API value of air pollutant X in Table S1, respectively.  $I_{x, high}$  and  $I_{x, low}$  stand for the two values in the API grading limited value table that mostly approach to value  $I_x$ , respectively.  $C_{x, high}$  and  $C_{x, low}$  represent the concentration of X corresponding to  $I_{x, high}$  and  $I_{x, low}$ , respectively. And the daily API value is defined as  $API = \text{Max}(I_{PM10}, I_{SO2}, I_{NO2}, I_{CO}, I_{O3})$ . According to API data records from March 20 to 23, 2010, PM<sub>10</sub> was the premier air pollutant in most of the 86 cities over China, i.e.  $API = I_{PM10}$ . Thus, the API value can be converted to PM<sub>10</sub> concentration as  $C = (I - I_{low})(C_{high} - C_{low}) / (I_{high} - I_{low}) + C_{low}$ . It should be noted that API was recorded with a maximum value of 500, which corresponded to the PM<sub>10</sub> concentration of 600  $\mu\text{g}/\text{m}^3$ .

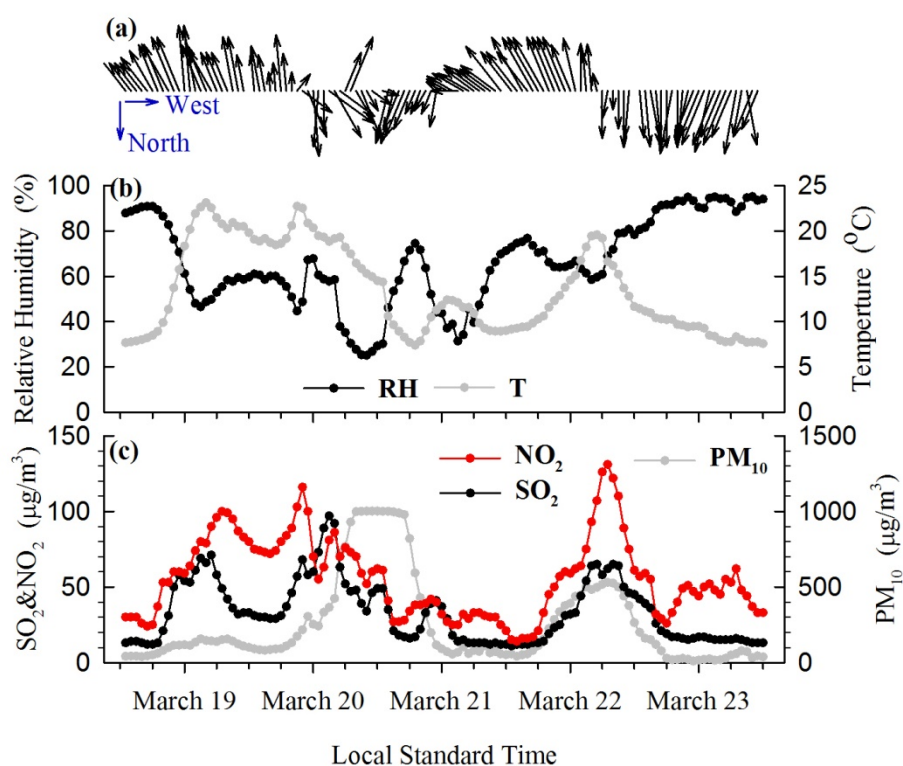
4. Figure 3, please add the description of the x axis that if it is local time or UTC, it

sometimes make me confused.

Thanks for the suggestion. Local time is used in this study. It is now indicated clearly in the caption of Figure 3.

5. Figure 4, I suggest that you can add the direction of north to south and east to west to give a clear direction of the wind.

Thanks for the suggestion. Figure 4 is revised as below.



6. Line 288, in Fig. 4c there are obviously decrease of NO<sub>2</sub> and SO<sub>2</sub> before they increase to the maximum during 6-18 on March 19.

Thanks for the comment. As shown in Fig. 4c, the concentrations of NO<sub>2</sub> and SO<sub>2</sub> indeed synchronously decreased before their maximum. This was partly attributed to the prevailing southeast winds, i.e. sea breezes which had clean effects on the local pollution. Furthermore, the decrease of NO<sub>2</sub> and SO<sub>2</sub> occurred during night from 18 LST of March 19 to 6 LST of March 20, when the anthropogenic emissions were relatively low during a day.

The related paragraph is revised as below.

As shown in Fig. 4a, the winds prevailed from the south before the onset of DS1 at ~10:00LST, March 20. Starting from early morning of March 19, SO<sub>2</sub> and NO<sub>2</sub> continuously climbed up due to the enhanced human activities. From 18:00 LST of

March 19 to 6:00 LST of March 20, the concentrations of NO<sub>2</sub> and SO<sub>2</sub> synchronously decreased. This was partly attributed to the prevailing southeast winds, i.e. sea breezes which had clean effects on the local pollution. Furthermore, the decrease of NO<sub>2</sub> and SO<sub>2</sub> occurred during night, when the anthropogenic emissions were relatively low during a day. During this period, SO<sub>2</sub> and NO<sub>2</sub> concentrations were relatively high with mean concentrations of  $39 \pm 19$  and  $70 \pm 25 \mu\text{gm}^{-3}$ , respectively.

**7. Line 389, why the number of Ca<sup>2+</sup> in DS1 is larger than that in DS1, although the intensity of DS1 was much stronger than DS2?**

Thanks for the comment. The abundance of Ca<sup>2+</sup> during the dust episodes depended on both the intensity of dust and the reaction efficiency of the insoluble CaCO<sub>3</sub> to the soluble Ca<sup>2+</sup>. Although the intensity of DS1 was much stronger than DS2, the concentrations of Ca<sup>2+</sup> in DS2 were comparable to that in DS1 (Fig. 6b), while the mass ratios of Ca<sup>2+</sup> in TSP were even higher in DS2 than in DS1 (Fig. 6d). This was mainly attributed to that more calcium in its soluble form (e.g. Ca(NO<sub>3</sub>)<sub>2</sub> and CaSO<sub>4</sub>) was produced via the reactions between calcium carbonate and acids. Particularly, higher concentrations and mass ratios of NO<sub>3</sub><sup>-</sup> in TSP in DS2 were observed than in DS1 (Fig. 6a&c), indicating more Ca(NO<sub>3</sub>)<sub>2</sub> was formed in DS2 than in DS1. Moreover, the ratio of Ca<sup>2+</sup>/Ca was higher in DS2 (0.2-0.5) than in DS1 (0.1-0.2) (Fig.7a), indicating a higher fraction of calcium carbonate from dust particles was transformed to soluble calcium.

**8. Line 465, I suppose the ratio of “[NH<sub>4</sub><sup>+</sup>+Ca<sup>2+</sup>]/[SO<sub>4</sub><sup>2-</sup>+NO<sub>3</sub><sup>-</sup>]” should be change into “[NH<sub>4</sub><sup>+</sup>+Ca<sup>2+</sup>+Mg<sup>2+</sup>]: : :” as Fig.7 shows.**

Thanks for pointing out this. It should be  $[\text{NH}_4^+ + \text{Ca}^{2+} + \text{Mg}^{2+}]/[\text{SO}_4^{2-} + \text{NO}_3^-]$  in Line 465.

In the revised version Line 465-472 was corrected as “We further investigated the  $[\text{NH}_4^+ + \text{Ca}^{2+} + \text{Mg}^{2+}]/[\text{SO}_4^{2-} + \text{NO}_3^-]$  ratio. As shown in Fig. 7d, with the addition of Ca<sup>2+</sup> and Mg<sup>2+</sup>, sulfate and nitrate had been completely neutralized, implying the important role of alkaline calcium and magnesium as the medium of dust heterogeneous reactions. By estimating the neutralization efficiency of Ca<sup>2+</sup> and Mg<sup>2+</sup> (NE<sub>Ca&Mg</sub>) as  $\text{NE}_{\text{Ca\&Mg}} = 1 - [\text{NH}_4^+]/[\text{SO}_4^{2-} + \text{NO}_3^-]$ , the average value of NE<sub>Ca&Mg</sub> in DS1 and DS2 was 0.34 and 0.50, respectively. The higher NE<sub>Ca&Mg</sub> in DS2 also suggested the chemical processing via dust was efficient under the environmental conditions such as DS2 in this study.”

**9. Line, 576, from the Fig. 9d, I also see there is a high mineral aerosols center at Gobi Desert, but the satellite can't show the same phenomenon. Please explain it.**

Thanks for pointing out this. As the satellite data is at daily resolution, the missing values of OMI Aerosol Index shown in the figure were mainly due to the gaps between the satellite swaths. If the swath width didn't cover the Gobi Desert, e.g. on

March 20 & 22, high spots of OMI Aerosol Index were not shown over the target region. When the satellite swath passed over the Gobi Desert on March 21, we did see high values of Aerosol Index over the Mongolian Gobi Desert and this was relatively consistent with the mineral dust simulation.

However, based on the definition of Aerosol Index, it is a parameter based on the difference between radiance at two near ultraviolet wavelengths. Thus, the comparison between satellite Aerosol Index and simulated mineral dust is only qualitative.

In the revised manuscript, we have indicated this in the second paragraph of Section 3.6.

**10. I would recommend the authors include and discuss these studies about dust transport over East Asia especially in March 2010 in the introduction.**

Thanks for the suggestion. We have included and discussed these studies in the introduction in the revised version.

Asian dust originating from the arid and semiarid areas in Mongolia and China can be transported for long distances, reaching Beijing (Sun et al., 2010), Shanghai (Fu et al., 2010), Xiamen (Zhao et al., 2011), Taiwan (Tsai et al., 2012; Tsai et al., 2014), and even as far as North America (Uno et al., 2009; Wu et al., 2015), exerting significant impacts on the air quality of both densely populated habitations and remote regions. Huang et al. (2014) showed that Asian dust could transport from the Qilian Mountain or from the Qaidam Basin through Qinghai and Gansu provinces to reach the Pacific Ocean, and that dust originating from the Taklimakan Desert could travel across the Hexi Corridor and Loess Plateau to reach southeastern China. Zhao et al. (2009) demonstrated that the deserts in Mongolia and in western and northern China were the major sources of Asian dust particles in East Asia and estimated that 26% of the dust particles emitted from Asian dust sources was transported to the Pacific Ocean. Eguchi et al. (2009) reported that the dust plume from the Gobi Desert in East Asia was transported at low altitudes of 4-6km to North America and mixed with Asian anthropogenic air pollutants during its transport. Fu et al. (2014) simulated that during a dust event from May 1 to 6, 2011, the transported dust particles accounted for 78.9% of the surface layer PM<sub>10</sub> over the Yangtze River Delta.

Dust aerosols can significantly influence the regional/global climate directly by absorbing and scattering solar radiation (Bi et al., 2016) and also indirectly by influencing the formation of ice nuclei, cloud, and precipitation (Creamean et al., 2013; Li and Min, 2010; Wang et al., 2010). In addition, deposition of transported dust aerosols into the ocean can enhance phytoplankton blooms due to the existence of bioavailable iron (Wang et al., 2012; Zhuang et al., 1992), which indirectly impacts on global climate change. The effects of dust aerosols on climate change depend critically on their physical and chemical properties. Natural dust aerosols with limited contamination have low light-absorption, with single-scattering albedo of 0.91-0.97 at 500nm and 550nm (Bi et al., 2014; Uchiyama et al., 2005). During the long-range transport, dust aerosols are often modified by their mixing with anthropogenic emissions over the downwind areas (Fischer et al., 2011; Formenti et al., 2011; Huang

et al., 2010b; Tobo et al., 2010), resulting in high uncertainties in evaluating the climatic effects of dust aerosols. It was estimated that mineral dust had a radiative forcing of  $-0.1 \pm 0.2 \text{ Wm}^{-2}$  (IPCC, 2013), of which the uncertainty was as high as 200%. Obviously, the characteristics of dust particles and their evolution during the transport are not well understood.

In March 2010, a super dust storm swept China, invading extensive areas from Northern China to Southern China including Fujian and Guangdong provinces, and lasting for ~4 days from March 19 to 23 (Li et al., 2011). The dust plumes further extended to the South China Sea (Wang et al., 2011), Taiwan (Tsai et al., 2013), Korea (Tatarov et al., 2012), Japan (Zaizen et al., 2014), and even to North America (Wu et al., 2015). This dust storm was as strong as the one in March 20-21, 2002 and attracted considerable attentions. Chen et al. (2017) used WRF-Chem to simulate the emission and transport of dust particles over the Taklimakan Desert and Gobi Desert. The results indicated that the Gobi Desert dust particles were easily lifted to 4km and subject to the long-range transport, which contributed much more to the dust plumes over East Asia than the Taklimakan Desert dust. Lidar observations revealed that this super dust storm was transported within a low altitude (Tatarov et al., 2012; Wang et al., 2011), which could benefit the mixing and interaction between dust particles and anthropogenic pollutants. Indeed, modifications of dust particles during the transport of this dust storm were suggested based on in situ measurements. Zhao et al. (2011) displayed substantial increases of particulate sulfate and nitrate when the dust plumes arrived at Xiamen city of Fujian province, implying the mixing and interaction between dust particles and anthropogenic pollutants. Wang et al. (2011) indicated that the dust particles detected at the Dongshan Island over the South China Sea were mixed with anthropogenic and marine particles. Observations of this dust storm at Tsukuba and Mt. Haruna, Japan showed that most of the transported dust particles in lower altitudes were internally mixed with sulfate or seasalt (Zaizen et al., 2014).

#### References:

- Zhao, T.L., S. L. Gong, X. Y. Zhang, et al., 2006: A Simulated Climatology of Asian Dust Aerosol and Its Trans-Pacific Transport. Part I: Mean Climate and Validation. *J. Climate.*, 19,88–103. doi: <http://dx.doi.org/10.1175/JCLI3605.1>.
- Eguchi, K., I. Uno, K. Yumimoto, et al., 2009: Trans-pacific dust transport: integrated analysis of NASA/CALIPSO and a global aerosol transport model. *Atmos. Chem. Phys.*, 9, 3137-3145.
- Fu, X., S. X. Wang, Z. Cheng, J. Xing, B. Zhao, J. D. Wang, and J. M. Hao, 2014: Source, transport and impacts of a heavy dust event in the Yangtze River Delta, China, in 2011. *Atmos. Chem. Phys.*, 14, 1239–1254.
- Huang J., T. Wang, W. Wang, Z. Li, and H. Yan, 2014: Climate effects of dust aerosols over East Asian arid and semiarid regions. *J. Geophys. Res.: Atmospheres*, 119, 11398-11416.
- Chen S., J. Huang, L. Kang, H. Wang, X. Ma, Y. He, T. Yuan, B. Yang, Z. Huang, and G. Zhang (2017). Emission, transport and radiative effects of mineral dust from Taklimakan and Gobi Deserts: comparison of measurements and model results. *Atmospheric Chemistry and Physics*, 17(3):1-43, doi: 10.5194/acp-17-2401-2017.



## Response to Comments from Anonymous Referee #2

The paper describes an interesting case study on interaction between dust and air pollution. The measurements of water-soluble ions showing heterogeneous reactions are especially interesting. I feel the subject is similar to that described in Pan et al., recently, though the observation methods are different. Pan et al. showed the change in morphology of dust by interaction with air pollution in Beijing (Pan et al., 2017, Real-time observational evidence of changing Asian dust morphology with the mixing of heavy anthropogenic pollution, *Scientific Reports* 7, 335, doi:10.1038/s41598-017-00444-w). I think it would be better to cite the paper and give a discussion.

We thank the reviewer for his/her careful reading of our manuscript and the supportive comments. We address the referee's specific comments as below. Please check the highlighted sentences in the revised manuscript for those changes.

The paper (Pan et al., 2017) recommended by the reviewer is now cited and discussed in the revision as "(Line 434) ...due to the heterogeneous reactions. Recently, Pan et al. (2017) reported that the concentrations of both  $\text{NO}_3^-$  and  $\text{Ca}^{2+}$  increased in coarse mode mineral dust in Beijing, particularly at high RH condition due to the interaction between nitric acid and Ca-rich particles. It is further suggested that the impact of nitrate on modifying the morphology of dust particles have become increasingly important, as the  $\text{NO}_x$  emissions in East Asia have been rapidly increasing."

1. What is the definition of the depolarization ratio (DR)? Is it volume depolarization ratio (total depolarization ratio)? or particle depolarization ratio (aerosol depolarization ratio)? They are different and should not be confused. Depolarization ratio shown in Fig. 3 is probably volume depolarization ratio (including molecular scattering), but the particle depolarization ratio must be used in the analysis for partitioning dust and non-dust particles.

Thanks for pointing out this issue. The depolarization ratio shown in Fig. 3 is indeed volume depolarization ratio ( $\delta v$ ), which is used to qualitatively identify the occurrence of dust events. When partitioning dust from non-dust particles, the particle depolarization ratio ( $\delta p$ ) has been applied. In the revised manuscript,  $\delta v$  and  $\delta p$  are clearly defined.

The first paragraph in Section 3.2 is revised as "Fig. 3a shows the time-height cross-section of  $\delta v$  (volume depolarization ratio) measured at the wavelength of 532 nm from March 19 to 23 in Shanghai.  $\delta v$  is frequently used to identify dust events and a threshold value of 10% is used to distinguish dust from other types of particles (Shimizu et al., 2004). As shown in Fig. 3a, there were evidently two discontinuous periods with  $\delta v$  higher than 10%, consistent with the two peaks of  $\text{PM}_{10}$  concentrations measured near the ground (Fig. 4c). The first dust episode (DS1) started from ~16:00 LST, March 20 to ~10:00LST, March 21 and the second dust

episode (DS2) started from ~6:00 LST, March 22 to ~0:00 LST, March 23.”

**2. Is the measured volume depolarization ratio calibrated? It is essential if the authors discuss the value of the particle depolarization ratio. It is also essential for partitioning dust and non-dust.**

Thanks for the comment. Yes, the observed signals used to calculate volume depolarization ratio ( $\delta v$ ) have been calibrated before the calculation. Briefly, a sheet polarizer with the polarizing direction set at 45 degree (then -45 degree) to the polarizing plane of the emitted light was installed in front of the beam splitter cube, and two sets of backscatter signal profiles from the sky were obtained for the calibration. Detailed calibration procedure has been described in Shimizu et al. (2004) and Shimizu et al. (2017).

Section 2.1.1 is revised as “A dual-wavelength depolarization Lidar (Model:L2S-SMII) developed by the National Institute for Environmental Studies (NIES) of Japan was installed on the roof (~20m above ground level ) of a teaching building on the campus of Fudan University in the Yangpu District of Shanghai (Fig. 1b). The Lidar measurement was performed every 15 min (at 00, 15, 30, and 45 minutes every hour) with a height resolution of 6 m. Attenuated backscattering coefficient ( $\beta$ ), volume depolarization ratio ( $\delta v$ ), particle depolarization ratio ( $\delta p$ ), and particle extinction coefficient ( $\sigma$ ) at the wavelength of 532 nm were obtained by the measurement. More details about the Lidar system have been described in Huang et al. (2012).  $\delta v$  is calculated using the parallel ( $I_p$ ) and perpendicular ( $I_s$ ) components of backscatter intensity, and  $I_p$  and  $I_s$  were calibrated before the calculation. Briefly, a sheet polarizer with the polarizing direction set at 45 degree (then -45 degree) to the polarizing plane of the emitted light was installed in front of the beam splitter cube, and two sets of backscatter signal profiles from the sky were obtained for the calibration. Detailed calibration procedure has been described in Shimizu et al. (2004) and Shimizu et al. (2017).  $\sigma$  was derived by the Fernald inversion method (Fernald, 1984) with the lidar ratio (extinction-to-backscatter ratio) set as 50 sr (Liu et al., 2002) in the inversion process. The total aerosol extinction coefficient can be split to non-spherical particle (dust particle,  $\sigma_d$ ) and spherical particle (mostly pollution particle,  $\sigma_s$ ) fractions based on the value of  $\delta p$ . The splitting method has been described in detail by Sugimoto et al. (2002) and Shimizu et al. (2004).

To solve the problem that overlap of the laser beam and the view field of telescope is insufficient for near surface observation, a compensation function  $Y(z)$  was applied. Function  $Y(z)$  was derived from the signal profiles that observed on a day when the planetary boundary layer was well developed. With the compensation, the optical properties of the particles above 120 m altitude were provided. Detailed correction procedure has been described in Shimizu et al. (2017).”

**3. Is the correction to the geometrical form factor (overlap function) applied? The decrease of the extinction coefficient near the surface in Fig. 8 seems not true. The**



correction should be applied if not. Unreliable part of the figure should be masked at least.

Thanks for the comment. To solve the problem that overlap of the laser beam and the view field of telescope is insufficient for near surface observation, a compensation function  $Y(z)$  was applied. Function  $Y(z)$  was derived from the signal profiles that observed on a day when the planetary boundary layer was well developed. With the compensation, the optical properties of the particles above 120 m altitude were provided. Detailed correction procedure has been described in Shimizu et al. (2017).

The vertical profiles shown in Fig. 8 have been revised starting from the altitude of 150 m, with unreliable data below 150 m excluded as suggested.

We have added this paragraph in Section 2.1.1 as shown above in last specific comment.

4. What is reason to show attenuated backscattering coefficient (BSC) in Fig. 8? It doesn't make sense to me. Dust extinction coefficient, non-dust extinction coefficient, and total extinction coefficient (dust + non-dust) should be indicated in the upper panels. The depolarization ratio in the lower panels must be the particle depolarization ratio.

Thanks for the comment. Fig. 8 is revised as suggested that the attenuated backscattering coefficient is replaced by the total extinction coefficient and the particle depolarization ratio is used in the lower panels.

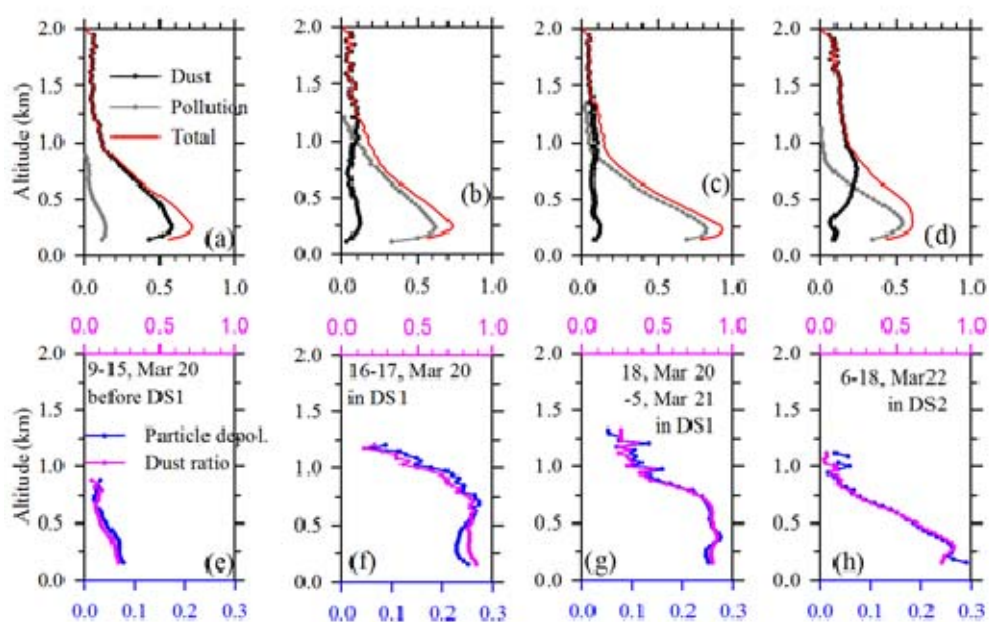


Fig.8 Vertical profiles of the average extinction coefficients of dust, pollution, and total particles ( $\text{km}^{-1}$ ), particle depolarization ratios (Particle depol., unitless), and the ratio of the dust extinction in the total extinction (Dust ratio, unitless) in four periods of 9:00 - 15:00 of March 20 (before DS1), 16:00 - 17:45 of March 20 (before the highest  $\text{PM}_{10}$  concentration in DS1), 18:00 of March 20 - 04:45 of March 21 (during the highest  $\text{PM}_{10}$  concentration in DS1), and 6:00 - 18:00 of March 22 in DS2.

1 Environmentally dependent dust chemistry of a super Asian dust storm in  
2 March 2010: observation and simulation

3

4 Qiongzhen Wang<sup>1, 2</sup>, Xinyi Dong<sup>3</sup>, Joshua S. Fu<sup>3</sup>, Jian Xu<sup>1</sup>, Congrui Deng<sup>1</sup>, Yilun  
5 Jiang<sup>1</sup>, Qingyan Fu<sup>4</sup>, Yanfen Lin<sup>4</sup>, Kan Huang<sup>1,5\*</sup>, Guoshun Zhuang<sup>1\*</sup>

6 <sup>1</sup>Center for Atmospheric Chemistry Study, Shanghai Key Laboratory of Atmospheric  
7 Particle Pollution and Prevention (LAP3), Department of Environmental Science and  
8 Engineering, Fudan University, Shanghai, 200433, P. R. China

9 <sup>2</sup>Environmental Science Research & Design Institute of Zhejiang Province, Hangzhou,  
10 310007, P. R. China

11 <sup>3</sup>Department of Civil and Environmental Engineering, University of Tennessee,  
12 Knoxville, TN, 37996, USA

13 <sup>4</sup>Shanghai Environmental Monitoring Center, Shanghai, 200030, China

14 <sup>5</sup>Institute of Atmospheric Sciences, Fudan University, Shanghai, 200433, P. R. China

15

16 Correspondence: huangkan@fudan.edu.cn; gzhuang@fudan.edu.cn

17

18 **Abstract**

19 Near surface and vertical *in situ* measurements of atmospheric particles were  
20 conducted in Shanghai during March 19-23, 2010 to explore the transport and  
21 chemical evolution of dust particles in a super dust storm. An air quality model with  
22 optimized physical dust emission scheme and newly implemented dust chemistry was  
23 utilized to study the impact of dust chemistry on regional air quality. Two  
24 discontinuous dust periods were observed with one travelling over Northern China  
25 (DS1) and the other passing over the coastal regions of Eastern China (DS2). Stronger  
26 mixing extents between dust and anthropogenic emissions were found in DS2,  
27 reflecting by the higher SO<sub>2</sub>/PM<sub>10</sub> and NO<sub>2</sub>/PM<sub>10</sub> ratios as well as typical pollution  
28 elemental species such as As, Cd, Pb, and Zn. As a result, the concentrations of SO<sub>4</sub><sup>2-</sup>

29 and  $\text{NO}_3^-$  and the ratio of  $\text{Ca}^{2+}/\text{Ca}$  were more elevated in DS2 than in DS1 but  
30 opposite for the  $[\text{NH}_4^+]/[\text{SO}_4^{2-}+\text{NO}_3^-]$  ratio, suggesting the heterogeneous reactions  
31 between calcites and acid gases were significantly promoted in DS2 due to the higher  
32 level of relative humidity and gaseous pollution precursors. Lidar observation showed  
33 a columnar effect on the vertical structure of **particle** optical properties in DS1 that  
34 dust dominantly accounted for ~80-90% of the total **particle** extinction from near the  
35 ground to ~700m. In contrast, the dust plumes in DS2 were refrained within lower  
36 altitudes while the extinction from **spherical** particles exhibited maximum at a high  
37 altitude of ~800m. The model simulation reproduced relatively consistent results with  
38 observations that strong impacts of dust heterogeneous reactions on secondary aerosol  
39 formation occurred in areas where the anthropogenic emissions were intensive.  
40 Compared to the sulfate simulation, the nitrate formation on dust is suggested to be  
41 improved in the future modeling efforts.

42

## 43 **1. Introduction**

44 Asian dust originating from the arid and semiarid areas in Mongolia and China can  
45 be transported for long distances, reaching Beijing (Sun et al., 2010), Shanghai (Fu et  
46 al., 2010), Xiamen (Zhao et al., 2011), Taiwan (Tsai et al., 2012; Tsai et al., 2014), and  
47 even as far as North America (Uno et al., 2009; Wu et al., 2015), exerting significant  
48 impacts on the air quality of both densely populated habitations and remote regions.  
49 Huang et al. (2014) showed that Asian dust could transport from the Qilian Mountain  
50 or from the Qaidam Basin through Qinghai and Gansu provinces to reach the Pacific  
51 Ocean, and that dust originating from the Taklimakan Desert could travel across the  
52 Hexi Corridor and Loess Plateau to reach southeastern China. Zhao et al. (2009)  
53 demonstrated that the deserts in Mongolia and in western and northern China were the  
54 major sources of Asian dust particles in East Asia and estimated that 26% of the dust  
55 particles emitted from Asian dust sources was transported to the Pacific Ocean.  
56 Eguchi et al. (2009) reported that the dust plume from the Gobi Desert in East Asia

57 was transported at low altitudes of 4-6km to North America and mixed with Asian  
58 anthropogenic air pollutants during its transport. Fu et al. (2014) simulated that during  
59 a dust event from May 1 to 6, 2011, the transported dust particles accounted for  
60 78.9% of the surface layer PM<sub>10</sub> over the Yangtze River Delta.

61 Dust particles can significantly influence the regional/global climate directly by  
62 absorbing and scattering solar radiation (Bi et al., 2016) and also indirectly by  
63 influencing the formation of ice nuclei, cloud, and precipitation (Creamean et al.,  
64 2013; Li and Min, 2010; Wang et al., 2010). In addition, deposition of transported  
65 dust particles into the ocean can enhance phytoplankton blooms due to the existence  
66 of bioavailable iron (Wang et al., 2012; Zhuang et al., 1992), which indirectly impacts  
67 on global climate change. The effects of dust particles on climate change depend  
68 critically on their physical and chemical properties. Natural dust particles with limited  
69 contamination have low light-absorption, with single-scattering albedo of 0.91-0.97 at  
70 500nm and 550nm (Bi et al., 2014; Uchiyama et al., 2005). During the long-range  
71 transport, dust particles are often modified by their mixing with anthropogenic  
72 emissions over the downwind areas (Fischer et al., 2011; Formenti et al., 2011; Huang  
73 et al., 2010b; Tobo et al., 2010), resulting in high uncertainties in evaluating the  
74 climatic effects of dust particles. It was estimated that mineral dust had a radiative  
75 forcing of  $-0.1 \pm 0.2 \text{ Wm}^{-2}$  (IPCC, 2013), of which the uncertainty was as high as  
76 200%. Obviously, the characteristics of dust particles and their evolution during the  
77 transport are not well understood.

78 In March 2010, a super dust storm swept China, invading extensive areas from  
79 Northern China to Southern China including Fujian and Guangdong provinces, and  
80 lasting for ~4 days from March 19 to 23 (Li et al., 2011). The dust plumes further  
81 extended to the South China Sea (Wang et al., 2011), Taiwan (Tsai et al., 2013), Korea  
82 (Tatarov et al., 2012), Japan (Zaizen et al., 2014), and even to North America (Wu et  
83 al., 2015). This dust storm was as strong as the one in March 20-21, 2002 and  
84 attracted considerable attentions. Chen et al. (2017) used WRF-Chem to simulate the

85 emission and transport of dust particles over the Taklimakan Desert and Gobi Desert.  
86 The results indicated that the Gobi Desert dust particles were easily lifted to 4km and  
87 subject to the long-range transport, which contributed much more to the dust plumes  
88 over East Asia than the Taklimakan Desert dust. Lidar observations revealed that this  
89 super dust storm was transported within a low altitude (Tatarov et al., 2012; Wang et  
90 al., 2011), which could benefit the mixing and interaction between dust particles and  
91 anthropogenic pollutants. Indeed, modifications of dust particles during the transport  
92 of this dust storm were suggested based on in situ measurements. Zhao et al. (2011)  
93 displayed substantial increases of particulate sulfate and nitrate when the dust plumes  
94 arrived at Xiamen city of Fujian province, implying the mixing and interaction  
95 between dust particles and anthropogenic pollutants. Wang et al. (2011) indicated that  
96 the dust particles detected at the Dongsha Island over the South China Sea were  
97 mixed with anthropogenic and marine particles. Observations of this dust storm at  
98 Tsukuba and Mt. Haruna, Japan showed that most of the transported dust particles in  
99 lower altitudes were internally mixed with sulfate or seasalt (Zaizen et al., 2014).

100 Most of the studies on this super dust storm focused on investigating the dust  
101 particles reaching Southeastern China and the South China Sea, and relied on single  
102 method, e.g. aerosol chemistry measurement, optical property inversion, or model  
103 simulation. In this study, we investigated this super dust storm in Shanghai, a coastal  
104 city in Eastern China. A synergy of measurement techniques was applied, including in  
105 situ measurements of pollutant gaseous precursors, particle with its major chemical  
106 components, and Lidar observation of particle optical properties. To corroborate the  
107 observational evidence, a regional numerical model was used to simulate the impact  
108 of dust chemistry on the perturbation of regional air quality. What interested us is that  
109 there were two discontinuous dust periods observed in Shanghai with distinctly  
110 different transport pathways, providing a great opportunity to study the chemical  
111 evolution of transported dust particles under different environmental conditions.

112



## 113 2. Methodology

### 114 2.1. Field measurement

#### 115 2.1.1. Lidar observation

116 A dual-wavelength depolarization Lidar (Model:L2S-SMII) developed by the  
117 National Institute for Environmental Studies (NIES) of Japan was installed on the roof  
118 (~20m above ground level ) of a teaching building on the campus of Fudan University  
119 in the Yangpu District of Shanghai (Fig. 1b). The Lidar measurement was performed  
120 every 15 min (at 00, 15, 30, and 45 minutes every hour) with a height resolution of 6  
121 m. Attenuated backscattering coefficient ( $\beta$ ), volume depolarization ratio ( $\delta v$ ), particle  
122 depolarization ratio ( $\delta p$ ), and particle extinction coefficient ( $\sigma$ ) at the wavelength of  
123 532 nm were obtained by the measurement. More details about the Lidar system have  
124 been described in Huang et al. (2012).  $\delta v$  is calculated using the parallel ( $I_p$ ) and  
125 perpendicular ( $I_s$ ) components of backscatter intensity, and  $I_p$  and  $I_s$  were calibrated  
126 before the calculation. Briefly, a sheet polarizer with the polarizing direction set at 45  
127 degree (then -45 degree) to the polarizing plane of the emitted light was installed in  
128 front of the beam splitter cube, and two sets of backscatter signal profiles from the sky  
129 were obtained for the calibration. Detailed calibration procedure has been described in  
130 Shimizu et al. (2004) and Shimizu et al. (2017).  $\sigma$  was derived by the Fernald  
131 inversion method (Fernald, 1984) with the lidar ratio (extinction-to-backscatter ratio)  
132 set as 50 sr (Liu et al., 2002) in the inversion process. The total particle extinction  
133 coefficient can be split to non-spherical particle (dust particle,  $\sigma_d$ ) and spherical  
134 particle (mostly pollution particle,  $\sigma_s$ ) fractions based on the value of  $\delta p$ . The splitting  
135 method was described in detail by Sugimoto et al. (2002) and Shimizu et al. (2004).

136 To solve the problem that overlap of the laser beam and the view field of telescope  
137 is insufficient for near surface observation, a compensation function  $Y(z)$  was applied.  
138 Function  $Y(z)$  was derived from the signal profiles that observed on a day when the  
139 planetary boundary layer was well developed. With the compensation, the optical  
140 properties of the particles above 120 m altitude were provided. Detailed correction

141 procedure has been described in Shimizu et al. (2017).

142

### 143 **2.1.2. Online particle and gases monitoring**

144 Continuous PM<sub>10</sub> concentrations were measured by a TEOM (Tapered Element  
145 Oscillating Microbalance) 1405D monitor (Thermo Scientific, USA). Trace gases SO<sub>2</sub>  
146 and NO<sub>2</sub> were measured by a 43i SO<sub>2</sub> analyzer (Thermo Scientific, USA) and a 42i  
147 NO-NO<sub>2</sub>-NO<sub>x</sub> analyzer (Thermo Scientific, USA), respectively. All the measured  
148 PM<sub>10</sub> and gases concentrations were averaged and used at intervals of 1hr in this  
149 study.

150

### 151 **2.1.3. Aerosol sampling**

152 TSP (Total Suspended Particles) samples were collected during March 19-27, 2010  
153 at the Fudan observational site co-located with all the other instruments. The aerosol  
154 samples were collected for 12 hours (normally from 8:00 to 20:00LST (Local  
155 Standard Time) in daytime and from 20:00 to 8:00 LST of the next day in nighttime)  
156 or 24 hours (normally from 8:00 to 8:00 LST of the next day) on Whatman 41 filters  
157 (Whatman Inc., Maidstone, UK) by a medium-volume sampler (Beijing Geological  
158 Instrument-Dickel Co., Ltd.; model: TSP/PM<sub>10</sub>/PM<sub>2.5</sub>-2; flow rate: 77.59 L min<sup>-1</sup>). All  
159 the samples were put in polyethylene plastic bags immediately after sampling and  
160 then reserved in a refrigerator. The filters were weighed before and after sampling  
161 using an analytical balance (Model: Sartorius 2004MP; reading precision: 10μg) after  
162 stabilizing in constant temperature (20±1°C) and humidity (40±2%) for 48 hours. All  
163 the procedures were strictly quality controlled to avoid the possible contamination of  
164 the samples.

165

## 166 **2.2. Chemical analysis**

### 167 **2.2.1. Ion analysis**

168 One fourth of each aerosol sample and blank filters were extracted ultrasonically by

169 10 ml deionized water ( $18 \text{ M}\Omega \text{ cm}^{-1}$ ). Inorganic ions of  $\text{SO}_4^{2-}$ ,  $\text{NO}_3^-$ ,  $\text{Cl}^-$ ,  $\text{Na}^+$ ,  $\text{NH}_4^+$ ,  
170  $\text{K}^+$ ,  $\text{Mg}^{2+}$ , and  $\text{Ca}^{2+}$  were analyzed by an Ion Chromatography (Dionex ICS 3000,  
171 USA) with a separation column of DionexIonpac AS 11, a guard column of Dionex  
172 Ionpac AG 11, a self-regenerating suppressed conductivity detector of Dionex Ionpac  
173 ED50, and a gradient pump of Dionex Ionpac GP50. The detailed analytical  
174 procedures can be found in Yuan et al. (2003).

175

### 176 **2.2.2. Element analysis**

177 Half of each aerosol sample and blank filters were digested at  $170 \text{ }^\circ\text{C}$  for 4 hours in  
178 a high pressure Teflon digestion vessel with 3ml concentrated  $\text{HNO}_3$ , 1ml  
179 concentrated  $\text{HClO}_4$ , and 1 ml concentrated HF. The solutions were dried, and then  
180 diluted to 10 ml with deionized water ( $18 \text{ M}\Omega \text{ cm}^{-1}$ ). Fifteen elements (Al, As, Ca, Cd,  
181 Cu, Fe, Mg, Mn, Na, Ni, Pb, Sr, Ti, V, and Zn) were measured by an inductively  
182 coupled plasma optical emission spectroscopy (ICP-OES; SPECTRO, Germany). The  
183 detailed analytical procedures were described in Sun et al. (2004a) and Zhuang et al.  
184 (2001).

185

### 186 **2.3. Nation-wide daily $\text{PM}_{10}$ data**

187 Air pollution index (API) data in 86 major cities (locations shown in Fig. 1a) over  
188 China were obtained from the data center of Ministry of Environmental Protection of  
189 China (<http://datacenter.mep.gov.cn/>). In China, six grades of air pollution of  
190 excellent, good, slightly polluted, lightly polluted, moderately polluted, and heavily  
191 polluted were set corresponding to the API scales of 0-50, 51-100, 101-150, 151-200,  
192 201-300, and  $>300$ , respectively. Both API values of 50, 100, 200, 300, 400, and 500  
193 and their corresponding concentrations of air pollutants were defined in the API  
194 grading limited value table as shown in Table S1. According to the definition of API  
195 in China, the API value of air pollutants was calculated as

$$196 \quad I_x = (I_{x, \text{high}} - I_{x, \text{low}})(C_x - C_{x, \text{low}})/(C_{x, \text{high}} - C_{x, \text{low}}) + I_{x, \text{low}},$$

197 where  $C_x$  and  $I_x$  are the concentration and the API value of air pollutant X in Table S1,  
198 respectively.  $I_{x, high}$  and  $I_{x, low}$  stand for the two values in the API grading limited value  
199 table (Table S1) that mostly approach to value  $I_x$ , respectively.  $C_{x, high}$  and  $C_{x, low}$   
200 represent the concentration of X corresponding to  $I_{x, high}$  and  $I_{x, low}$ , respectively. And  
201 the daily API value is defined as

$$202 \quad \text{API} = \text{Max}(I_{\text{PM}_{10}}, I_{\text{SO}_2}, I_{\text{NO}_2}, I_{\text{CO}}, I_{\text{O}_3}).$$

203 According to API data records from March 20 to 23, 2010,  $\text{PM}_{10}$  was the premier air  
204 pollutant in most of the 86 cities over China, i.e.  $\text{API} = I_{\text{PM}_{10}}$ . Thus, the API value can  
205 be converted to  $\text{PM}_{10}$  concentration as

$$206 \quad C = (I - I_{\text{low}})(C_{\text{high}} - C_{\text{low}})/(I_{\text{high}} - I_{\text{low}}) + C_{\text{low}}.$$

207 It should be noted that API was recorded with a maximum value of 500, which  
208 corresponded to the  $\text{PM}_{10}$  concentration of  $600 \mu\text{gm}^{-3}$ .

209

#### 210 **2.4. Backward trajectory analysis**

211 48 hours back trajectories of the air masses at both 250 m and 1000 m AGL (Above  
212 Ground Level) during dust days starting at Shanghai were computed by the HYSPLIT  
213 model (<http://ready.arl.noaa.gov/hypub-bin/trajtype.pl?runtype=archive>), using the  
214 meteorological data of GDAS (1 degree, global, 2006-present). Four trajectories  
215 ending at 0, 6, 12, and 18 LST were calculated for each day.

216

#### 217 **2.5. Model simulation**

218 The WRF/CMAQ modeling system was applied to simulate the dust chemistry in  
219 this study. The Weather Research and Forecasting model (WRFv3.4) was used to  
220 produce the meteorology fields by digesting the reanalysis data from National Centers  
221 for Environmental Prediction (NCEP). The Community Multiscale Air Quality  
222 Modeling System (CMAQv5.0.1) was configured with the 2005 carbon bond  
223 gas-phase mechanism (CB05) and aerosol module AE6. The default CMAQ model  
224 doesn't include dust chemistry reactions but only the dust emission module. We have

225 implemented dust chemistry in the CMAQ model and corrected the dust emission  
226 module in our earlier work (Dong et al., 2015), which was used to simulate the  
227 heterogeneous reactions on dust during the long-range transport in this study. Briefly,  
228 the major developments included: (1) The default dust emission module in CMAQ  
229 was found to strongly underestimate the dust emissions. By removing the double  
230 counting of soil moisture in the default dust emission module and conducting a  
231 reanalysis of field data, the threshold friction velocities over various land covers were  
232 re-adjusted. (2) The source-dependent speciation profiles of dust particles from the  
233 Taklimakan and Gobi Desert were implemented based on field measurement data. (3)  
234 Thirteen dust heterogeneous reactions were implemented, including dust reactions  
235 with O<sub>3</sub>, OH, H<sub>2</sub>O<sub>2</sub>, CH<sub>3</sub>COOH, CH<sub>3</sub>OH, CH<sub>2</sub>O, HNO<sub>3</sub>, N<sub>2</sub>O<sub>5</sub>, NO<sub>2</sub>, NO<sub>3</sub>, HO<sub>2</sub>, and  
236 SO<sub>2</sub>. The uptake coefficients of gases onto the surface of dust particles were taken  
237 from previous published studies in deserts of China. More details of the technical  
238 development of this dust emission and chemistry module in CMAQ and the  
239 evaluation of model performance can be found in Dong et al. (2015).

240 The modeling domain includes whole China with a horizontal grid resolution of 36  
241 km×36 km and 34 vertical layers with a model top at 50 hPa. The chemical initial and  
242 boundary conditions for CMAQ were downscaled from the GEOS-Chem global  
243 model. Emissions inputs included anthropogenic emissions from Zhao et al. (2013)  
244 over China, biogenic emissions from MEGAN2.1 (Guenther et al., 2006), and  
245 biomass burning emissions from FLAMBE (Reid et al., 2009).

246

### 247 **3. Results and Discussion**

#### 248 **3.1. Spatiotemporal evolution of the 2010 spring dust storm over China**

249 On March 19, 2010, a super dust storm outbreak over the Gobi Desert of Inner  
250 Mongolia, China and southern Mongolia. It was driven by a strong cold front and  
251 revealed evidently by the OMI (Ozone Monitoring Instrument) aerosol index (AI)  
252 from space detection (Tatarov et al., 2012). Along with the cold front, the dust plumes

253 moved southeastward, invading extensive areas from Northern China to Southern  
254 China. Fig. 2 shows the daily  $PM_{10}$  concentrations over 86 cities of China from March  
255 19 to 23, 2010, displaying the spatiotemporal evolution of this dust storm event. On  
256 March 20, daily  $PM_{10}$  concentrations of higher than  $200 \mu\text{gm}^{-3}$  were observed over  
257 widespread areas of Northern China, close to the dust source regions. The  $PM_{10}$   
258 concentrations of those heavily polluted cities, including Yinchuan (YC), Datong  
259 (DT), Hohhot (HHT), and Beijing (BJ) (red circles in Fig. 1a,) reached the threshold of  
260  $600 \mu\text{gm}^{-3}$ , the maximum value recorded by API (Fig. 2a). As the dust plumes  
261 transported, high levels of  $PM_{10}$  started to emerge over Central and Eastern China on  
262 March 21, when heavy pollution with daily  $PM_{10}$  concentrations higher than  
263  $420\mu\text{gm}^{-3}$  were observed over the Yangtze River Delta region as well as in Jiangxi,  
264 Hunan, and Hubei provinces. Specifically, the  $PM_{10}$  concentrations in Shanghai,  
265 Nanjing (NJ), Hefei (HF), Wuhan (WH), Hangzhou (HZ), and so on (blue circles in  
266 Fig. 1a) all reached the threshold of  $600 \mu\text{gm}^{-3}$  (Fig. 2c). On March 22 and 23, the  
267 dust plumes drifted towards Fujian and Guangdong provinces in Southern China,  
268 where  $PM_{10}$  concentrations of over  $600\mu\text{gm}^{-3}$  were even observed in coastal cities  
269 such as Fuzhou (FZ), Xiamen (XM), and Shantou (ST) (pink circles in Fig.1a). The  
270 severe air pollution over China caused by this super dust storm lasted for ~4 days  
271 until March 23, resulting in significant impacts on the regional air quality and possible  
272 perturbation on regional meteorology.

273

### 274 3.2. Identification of two dust plumes with distinct transport pathways

275 Fig. 3a shows the time-height cross-section of  $\delta v$  (volume depolarization ratio)  
276 measured at the wavelength of 532 nm from March 19 to 23 in Shanghai.  $\delta v$  is  
277 frequently used to identify dust events and a threshold value of 10% is used to  
278 distinguish dust from other types of particles (Shimizu et al., 2004). As shown in Fig.  
279 3a, there were evidently two discontinuous periods with  $\delta v$  higher than 10%,  
280 consistent with the two peaks of  $PM_{10}$  concentrations measured near the ground (Fig.



281 4c). The first dust episode (DS1) started from ~16:00 LST, March 20 to ~10:00LST,  
282 March 21 and the second dust episode (DS2) started from ~6:00 LST, March 22 to  
283 ~0:00 LST, March 23.

284 The 48-hours backward trajectories of the air masses during March 20-23 in  
285 Shanghai are shown in Fig. 2. It is interesting to note that the transport pathways of  
286 the dust plumes in DS1 and DS2 were distinctly different. In DS1, the dust plumes at  
287 both low altitudes (i.e. 250m denoted by the black lines in Fig. 2c-d) and high  
288 altitudes (i.e. 1000m denoted by the red lines in Fig. 2c-d) were mostly transported  
289 from the dust source regions in the Gobi Desert. This is one of the typical inland  
290 transport pathways of Asian dust, which passed over Northern China that is  
291 characterized of intense anthropogenic emission rates, e.g. from Shanxi, Hebei, and  
292 Shandong provinces.

293 In DS2, the air masses reaching Shanghai are shown in Fig. 2e – h. From the  
294 starting of DS2 to the midday of March 22 (Fig. 2e-f), the backward trajectories were  
295 still mainly from the north but we noticed that the low altitude trajectories which  
296 originated from the Gobi Desert travelled over the Yellow Sea and East China Sea  
297 and then circled back to Shanghai. After the midday of March 22 (Fig. 2g-h), the  
298 trajectories became much shorter and restricted within the costal and offshore areas.  
299 The low-altitude trajectories were mainly from the ocean and the high-altitude  
300 trajectories shifted from the south. As indicated by the surface observation (Fig. 4a),  
301 the southeasterly winds prevailed until ~18:00 LST, March 22 when  $PM_{10}$  climbed to  
302 reach its peak value in DS2, quite different from DS1 when the northerly winds  
303 dominated. The CALIPSO (Cloud-Aerosol Lidar and Infrared Pathfinder Satellite  
304 Observations) transect at around 13:00 – 13:30 LST, March 21 specified that the  
305 major aerosol type was dust over the East China Sea and South China Sea (Fig. S1).  
306 Therefore, it was evident that DS2 passed over the coastal regions of Eastern China  
307 and the ocean and it should be a humid dust plume.

308 As visualized in Fig. 3, the two dust plumes were mostly transported at low

309 altitudes below 1km. It is expected that this type of transport would benefit for the  
310 mixing and interactions between dust particles and anthropogenic pollutants, as the  
311 anthropogenic emissions were mainly trapped within the boundary layer. Transport  
312 pathway is one of the most important factors accounting for the evolution of dust  
313 particles and the resulting environmental effects (Zaizen et al., 2014; Zhang et al.,  
314 2010). In this super dust storm, the two discontinuous dust plumes reaching Shanghai  
315 were distinctly different in their transport pathways, providing a great opportunity to  
316 study the chemical evolution of dust particles under different transport conditions.

317

### 318 **3.3. Distinct behaviors of gaseous pollutants between two dust episodes**

319 Fig. 4 illustrates the different behaviors of the two identified dust episodes by  
320 plotting the temporal variations of emission precursors (i.e. SO<sub>2</sub> and NO<sub>2</sub>) as well as  
321 PM<sub>10</sub> and crucial meteorological parameters. As shown in Fig. 4a, the winds prevailed  
322 from the south before the onset of DS1 at ~10:00LST, March 20. Starting from early  
323 morning of March 19, SO<sub>2</sub> and NO<sub>2</sub> continuously climbed up due to the enhanced  
324 human activities. From 18:00 LST of March 19 to 6:00 LST of March 20, the  
325 concentrations of NO<sub>2</sub> and SO<sub>2</sub> synchronously decreased. This was partly attributed to  
326 the prevailing southeast winds, i.e. sea breezes which had clean effects on the local  
327 pollution. Furthermore, the decrease of NO<sub>2</sub> and SO<sub>2</sub> occurred during night, when the  
328 anthropogenic emissions were relatively low during a day. During this period, SO<sub>2</sub>  
329 and NO<sub>2</sub> concentrations were relatively high with mean concentrations of  $39 \pm 19$  and  
330  $70 \pm 25 \mu\text{gm}^{-3}$ , respectively. In the meantime, PM<sub>10</sub> was at a moderate level of  $112 \pm$   
331  $54 \mu\text{gm}^{-3}$ , suggesting the dominance by anthropogenic emissions. It was observed that  
332 the peak hourly concentrations of SO<sub>2</sub> and NO<sub>2</sub> up to  $97 \mu\text{gm}^{-3}$  and  $116 \mu\text{gm}^{-3}$  occurred  
333 just a few hours before the sharp increase of PM<sub>10</sub>. This was due to that air pollutants  
334 north of Shanghai were pushed by the cold front and accumulated before the dust  
335 plumes invaded (Guo et al., 2004), which was also evident from the time difference  
336 between the values of  $\beta$  and  $\delta v$  as shown in Fig. 3.

337 From 10:00 LST, March 20 to 11:00 LST, March 21, the winds shifted from the  
338 north and northwest accompanied with a quick drop of relative humidity (RH) with a  
339 minimum of 25% at 21:00 LST, March 20, indicating the invasion of a strong cold  
340 front from Northern China. Correspondingly, PM<sub>10</sub> abruptly climbed since 16:00 LST  
341 and reached 1000 μgm<sup>-3</sup> (a maximum value of 1000 μgm<sup>-3</sup> was set in the TEOM  
342 1405D monitor) within four hours. This high level of PM<sub>10</sub> lasted for ~11 hours till  
343 04:00 LST, March 21. During this dust episode, the concentrations of SO<sub>2</sub> and NO<sub>2</sub>  
344 decreased substantially and the lowest values of 17 μgm<sup>-3</sup> and 27 μgm<sup>-3</sup> (Fig. 4c) were  
345 recorded at 04:00 LST, March 21, due to the strong dilution effect of dust plumes. The  
346 ratios of SO<sub>2</sub>/PM<sub>10</sub> and NO<sub>2</sub>/PM<sub>10</sub> were as low as 0.04 ± 0.02 and 0.06 ± 0.03 in DS1  
347 compared to that of 0.30 ± 0.05 and 0.57 ± 0.28 before DS1. After 12:00 LST, March  
348 21, the wind direction started to shift again from the southeast with an increase of RH.  
349 The PM<sub>10</sub> concentrations quickly decreased below 200 μgm<sup>-3</sup> within five hours,  
350 indicating the pass of the first dust episode over Shanghai.

351 The second wave of dust (DS2) commenced after about half a day as indicated by  
352 the temporal variation of PM<sub>10</sub> climbing quickly since 6:00 LST, March 22. PM<sub>10</sub>  
353 reached its peak of 530 μgm<sup>-3</sup> observed at ~18:00LST, March 22, much lower than the  
354 peak values during DS1. It should be noted that during the growth of DS2 (i.e. from  
355 06:00 to 18:00 LST), southerly winds sustained until 18:00 LST, March 22, opposite  
356 to DS1. As discussed above, DS2 had gone through the maritime environment during  
357 most of its transport trajectory. This can be corroborated by the moderately high RH  
358 (Fig. 4b). After 18:00 LST, March 22, PM<sub>10</sub> underwent a quick decline followed by  
359 the prevailing northeast winds and continuously elevated RH. This suggested the sea  
360 breezes after 18:00 LST were almost free of dust particles and acted as cleaner for the  
361 dust pollution that was previously accumulated. Compared to the mean RH of 46% ±  
362 18% in DS1, RH in DS2 was much higher of 69% ± 8%. This was mainly attributed  
363 to the different transport pathways of the two dust episodes.

364 One interesting phenomenon that has been rarely observed was that the temporal

365 variations of SO<sub>2</sub> and NO<sub>2</sub> varied fairly consistent with that of PM<sub>10</sub> in DS2 (Fig. 4c),  
366 quite different from DS1 and previous studies (Fu et al., 2010; Guo et al., 2004) that  
367 dust usually had a clean effect on the local gaseous pollutants, causing inverse  
368 relationship between SO<sub>2</sub>/NO<sub>2</sub> and PM<sub>10</sub>. In this case, NO<sub>2</sub> reached its maximum  
369 hourly concentration of 131 μg m<sup>-3</sup> along with the maximum PM<sub>10</sub> in DS2, the highest  
370 during the whole study period. This probably indicated that the dust particles in DS2  
371 were externally mixed or “coated” with abundant gaseous pollutants. As a result, the  
372 SO<sub>2</sub>/PM<sub>10</sub> and NO<sub>2</sub>/PM<sub>10</sub> ratios reached 0.11 ± 0.03 and 0.20 ± 0.04 in DS2,  
373 respectively, much higher than those in DS1 and in a super dust day of April 2, 2007  
374 in Shanghai (Fu et al., 2010), revealing that the dust plumes in DS2 were much more  
375 polluted.

376 In the following sections, we will investigate deeply into the chemical  
377 characteristics and evolution of the two dust episodes.

378

### 379 **3.4. Chemical evolution of dust particles**

#### 380 **3.4.1. Pollution elements significantly enhanced in dust periods**

381 Table 1 lists the concentrations of measured elements in TSP before, during, and  
382 after the two dust episodes in Shanghai. D and N represent the samples that collected  
383 in daytime (~8:00 to ~20:00 LST) and nighttime (~20:00 to 8:00 LST in the next day),  
384 respectively. NDS represents the non-dust days from March 25 to 27 and the mean  
385 concentrations are shown in Table 1. To identify whether these elements were mainly  
386 derived from the crustal source or anthropogenic sources, enrichment factors of  
387 elements were calculated. Enrichment factor (EF) is defined as  
388  $EF = (X/X_{Ref})_{particle} / (X/X_{Ref})_{crust}$ , where  $(X/X_{Ref})_{particle}$  is the mass ratio of a given  
389 element X to the reference element in **particle** and  $(X/X_{Ref})_{crust}$  is the ratio in the crust  
390 (Lida, 2006), and Al is the reference element used in this study. EFs of Al, Cu, Ca, Fe,  
391 Mg, Na, Mn, Ti, Sr, Ni, and V were calculated to be lower than 5, indicating these  
392 eleven elements were mostly from the crustal source, while EFs of As, Cd, Pb, and Zn

393 were higher than 10 even during the dust periods (Fig.5c), indicating these four  
394 elements were significantly influenced by anthropogenic sources. Hence, Al, Cu, Ca,  
395 Fe, Mg, Na, Mn, Ti, Sr, Ni, and V were classified as “crustal elements” while As, Cd,  
396 Pb, and Zn were classified as “pollution elements”. Due to the dilution effect of dust  
397 plumes, EFs of the four pollution elements decreased from ~100-150 in NDS to  
398 ~10-50 in DS1 and ~20-115 in DS2.

399 As shown in Table 1, the concentrations of the crustal elements before the dust  
400 event (19N) were as low as those in NDS, but substantially increased in DS1 and DS2,  
401 about 3-13 and 1-7 folds of those in NDS, respectively. The highest concentration of  
402 Al, widely used as a tracer for dust, reached  $67.5 \mu\text{g m}^{-3}$  in DS1 (20N), comparable to  
403 the Al concentration in the super dust day of April 2, 2007 in Shanghai (Fu et al.,  
404 2010). The highest concentrations of crustal elements in DS1 (20N) were ~2 folds of  
405 those in DS2 (22D), corroborating that the intensity of DS1 was stronger than in DS2.

406 As for the pollution elements, the non-crustal part (nc-) of As, Cd, Pb, and Zn were  
407 estimated as  $\text{nc-X} = X - \text{Al} \times (X/\text{Al})_{\text{crust}}$ . The concentrations of nc-As, nc-Cd, nc-Pb,  
408 and nc-Zn increased in both DS1 and DS2, about 1-4folds of those in NDS (Fig. 5a).  
409 As these elements were mainly derived from anthropogenic sources such as coal  
410 combustion, industrial processing, vehicle emissions, etc., their enhancement  
411 indicated that abundant pollutants had been transported to the downwind regions  
412 along with the dust plumes. The mean concentrations of nc-As, nc-Cd, nc-Pb, and  
413 nc-Zn were 23.5, 3.6, 154.2, and  $580.1 \text{ ng m}^{-3}$  in DS2, higher than those of 18.3, 3.1,  
414 119.7, and  $447.4 \text{ ng m}^{-3}$  in DS1, indicating DS2 was more polluted. Consistently, the  
415 mass ratios of nc-As, nc-Cd, nc-Pb, and nc-Zn in TSP were  $5.1 \times 10^{-3}\%$ ,  $7.2 \times 10^{-4}\%$ ,  
416  $3.1 \times 10^{-2}\%$ , and  $1.2 \times 10^{-1}\%$  in DS2, higher than those of  $1.9 \times 10^{-3}\%$ ,  $3.7 \times 10^{-4}\%$ ,  
417  $1.5 \times 10^{-2}\%$ , and  $6.2 \times 10^{-2}\%$  in DS1 (Fig. 5b).

418

### 419 3.4.2. Crustal vs. secondary water-soluble ions

420 Fig. 6 shows the evolution of major water-soluble ions in TSP during the whole

421 dust event. The concentrations of  $\text{Na}^+$ ,  $\text{K}^+$ ,  $\text{Mg}^{2+}$ , and  $\text{Ca}^{2+}$  increased the most among  
422 all the ions in both DS1 and DS2 due to their crustal origin, ~2-5 and ~2-3 folds of  
423 those in NDS. However, the mass ratios of these ions in TSP generally decreased in  
424 the dust periods (Fig. 6d), as the masses of dust particles were dominated by  
425 water-insoluble matters. Different from NDS, the concentrations of  $\text{Ca}^{2+}$  exceeded  
426  $\text{NH}_4^+$  and ranked as the most abundant cation in the dust periods. This was because  
427 Asian dust particles are rich of calcium carbonate (Wang et al., 2005), which could  
428 react with acidic nitrogen and sulfur compounds to form  $\text{Ca}(\text{NO}_3)_2$  and  $\text{CaSO}_4$ . It has  
429 been found Ca-rich particles in Asian dust transported to Japan were mostly in the  
430 spherical shape (Zaizen et al., 2014), and many of the spherical Ca-rich particles  
431 contained sulfur and nitrogen compounds (Matsuki et al., 2006; Zaizen et al., 2014)  
432 due to the heterogeneous reactions. Recently, Pan et al. (2017) reported that the  
433 concentrations of both  $\text{NO}_3^-$  and  $\text{Ca}^{2+}$  increased in coarse mode mineral dust in  
434 Beijing, particularly at high RH condition due to the interaction between nitric acid  
435 and Ca-rich particles. It is further suggested that the impact of nitrate on modifying  
436 the morphology of dust particles have become increasingly important, as the  $\text{NO}_x$   
437 emissions in East Asia have been rapidly increasing. It is noted that the concentrations  
438 of  $\text{Ca}^{2+}$  in DS2 were comparable to that in DS1 (Fig. 6b), although the intensity of  
439 DS1 was much stronger than DS2. In addition, the mass ratios of  $\text{Ca}^{2+}$  in TSP were  
440 even higher in DS2 than in DS1 (Fig. 6d). Collectively, these results indicated that  
441 more calcium in its soluble form was produced via the reactions between calcium  
442 carbonate and acids. This could be also revealed by the ratio of  $\text{Ca}^{2+}/\text{Ca}$  that was  
443 higher in DS2 (0.2-0.5) than in DS1 (0.1-0.2) (Fig.7a). In DS2, the dust plumes  
444 travelled over the ocean and carried higher amount of water vapor as well as  $\text{SO}_2$  and  
445  $\text{NO}_2$  than DS1 as discussed earlier. In this regard, the heterogeneous reaction between  
446 calcium carbonate and acidic gases was enhanced more in DS2, resulting in a higher  
447 fraction of calcium carbonate from dust particles that could be transformed to soluble  
448 calcium.



449 Cl<sup>-</sup> during the dust periods was moderately enhanced by ~1-2 folds compared to  
450 NDS, indicating that Cl<sup>-</sup> was also impacted by the invasion of dust plumes. As shown  
451 in Fig. 6a & 6c, both the concentrations of Cl<sup>-</sup> and its mass ratios in TSP were higher  
452 in DS2 than in DS1. As the air masses of DS2 passed over the ocean, part of the high  
453 Cl<sup>-</sup> concentrations should be attributed to the contribution from seasalts. The average  
454 equivalent ratio of Cl<sup>-</sup> to Na<sup>+</sup> ([Cl<sup>-</sup>]/[Na<sup>+</sup>]) was 1.65 in NDS and 2.17 in 19N, higher  
455 than the ratio in seawater (1.17), indicating that anthropogenic sources such as coal  
456 combustion (Sun et al., 2014; Yao et al., 2002) contributed significantly to Cl<sup>-</sup> in the  
457 non-dust days. The [Cl<sup>-</sup>]/[Na<sup>+</sup>] ratio dropped to ~1.0 in DS1 as massive continental  
458 particles invaded Shanghai, while in DS2 the ratio was elevated to 1.5. Thus, both  
459 seasalts and anthropogenic sources should contribute to the particulate Cl<sup>-</sup> in DS2.

460 As for the secondary inorganic ions (i.e. SO<sub>4</sub><sup>2-</sup>, NO<sub>3</sub><sup>-</sup>, and NH<sub>4</sub><sup>+</sup>), their  
461 concentrations in TSP were elevated to be 16.2, 15.4, and 7.2 μg m<sup>-3</sup> in the daytime of  
462 March 20 (20D) in DS1. The sampling time of 20D was from ~8:00 to 20:00 LST,  
463 including the short period of pollutants accumulation before the arrival of DS1. As a  
464 result, the high concentrations of SO<sub>4</sub><sup>2-</sup> and NO<sub>3</sub><sup>-</sup> measured in 20D were contributed  
465 from both local and transported sulfate and nitrate, as well as from the heterogeneous  
466 reactions on dust particles. In the nighttime of March 20 (20N), the concentrations of  
467 NO<sub>3</sub><sup>-</sup> and NH<sub>4</sub><sup>+</sup> sharply decreased by 57.8% and 43.2%, respectively. Although SO<sub>4</sub><sup>2-</sup>  
468 also decreased, its reduction extent was much weaker of 27.8% and was still ~2 folds  
469 of that in NDS (Fig. 6a). Nitrate formation on dust is strongly dependent on the  
470 ambient conditions. Low temperature, low relative humidity, strong wind and low  
471 concentrations of pollution gases did not favor the heterogeneous reaction (Huang et  
472 al., 2010a; Yuan et al., 2008). Hence, strong dust events usually diluted the  
473 concentrations of nitrate (Duvall et al., 2008; Huang et al., 2010a; Wang et al., 2006).  
474 As for the sulfate formation on dust, SO<sub>2</sub> could interact with various mineral  
475 components of dust particles to produce sulfate, and sulfate became mixed with the  
476 dust first competing with nitrate (Dupart et al., 2012; Sullivan et al., 2007). Hence,

477 although the secondary **particle** components were diluted by the invasion of dust, the  
478 formation of sulfate could still be compensated by the heterogeneous reaction on dust  
479 to some extent.

480 In the daytime of March 22 (22D) during DS2, the concentrations of  $\text{SO}_4^{2-}$  and  
481  $\text{NO}_3^-$  reached the highest during the study period with values of 16.6 and 19.3  $\mu\text{gm}^{-3}$ ,  
482 respectively. Although  $\text{SO}_4^{2-}$  and  $\text{NO}_3^-$  decreased in the nighttime of March 22 (22N),  
483 their levels were still higher than the non-dust days (Fig. 6a). Also, the mass ratios of  
484  $\text{SO}_4^{2-}$  and  $\text{NO}_3^-$  in TSP were higher in DS2 than DS1 (Fig. 6c). These results indicated  
485 that  $\text{SO}_4^{2-}$  and  $\text{NO}_3^-$  were more favorably formed in DS2. It was observed that the  
486 concentration of  $\text{NO}_3^-$  was even higher than that of  $\text{SO}_4^{2-}$  in both daytime and  
487 nighttime samples during DS2, showing a contrary behavior to DS1. As discussed  
488 above, the formation of nitrate on dust strongly depends on the ambient conditions.  
489 During DS2, RH was at a moderately high level, enhancing the efficiency of aqueous  
490 processing on the particles. In addition, the abnormally high concentrations of  $\text{NO}_2$   
491 (Fig. 4c) suggested the emission precursors were sufficient for the production of  
492 nitrate. Finally, high concentrations of nitrate during DS2 may be partially attributed  
493 to the reaction between sea salts and nitric acid (Hsu et al., 2014; Huang et al., 2010a)  
494 as the dust plumes travelled over the ocean. The formation of secondary aerosol  
495 species during DS2 should have involved the complex interactions between pollutant  
496 precursors, dust, and sea salts.

497 Fig. 7b shows the equivalent ratio of the total anions to the total cations (A/C) in  
498 TSP. The A/C ratio dropped to  $\sim 0.5$  in DS1 from  $\sim 0.9$  in 19N, which was attributed to  
499 the existence of abundant  $\text{CO}_3^{2-}$  in dust particles that can't be detected by Ion  
500 Chromatography (Huang et al., 2010a). The A/C ratio reached 0.85 and 0.80 in 22D  
501 and 22N in DS2, respectively, much higher than those in DS1, suggesting that more  
502 fraction of  $\text{CaCO}_3$  in the dust particles in DS2 was transformed to  $\text{CaSO}_4$  and  
503  $\text{Ca}(\text{NO}_3)_2$  than in DS1, consistent with the higher  $\text{Ca}^{2+}/\text{Ca}$  ratio in DS2 than in DS1  
504 (Fig. 7a). The equivalent ratio of  $\text{NH}_4^+$  to the sum of  $\text{SO}_4^{2-}$  and  $\text{NO}_3^-$  ( $[\text{NH}_4^+]/$

505  $[\text{SO}_4^{2-}+\text{NO}_3^-]$ ) in TSP also indicated that the heterogeneous reactions between  
506 carbonate and acid gases were more promoted in DS2 compared to DS1. As shown in  
507 Fig. 7c, the  $[\text{NH}_4^+]/[\text{SO}_4^{2-}+\text{NO}_3^-]$  ratio was slightly higher than one in the non-dust  
508 days, indicating that  $\text{SO}_4^{2-}$  and  $\text{NO}_3^-$  could be completely neutralized by  $\text{NH}_4^+$ . In DS1,  
509 the  $[\text{NH}_4^+]/[\text{SO}_4^{2-}+\text{NO}_3^-]$  ratio was 0.68 and 0.65 in 20D and 20N, while in DS2 it was  
510 even lower of 0.45 and 0.55 in 22D and 22N, respectively. Apparently,  $\text{NH}_4^+$  was  
511 insufficient for completely neutralizing  $\text{SO}_4^{2-}$  and  $\text{NO}_3^-$  in both dust episodes,  
512 particularly in DS2. The ammonium deficiency was also observed in Kinmen and  
513 Zhuhai (Hsu et al., 2014), an island site and a coastal site, respectively, during this  
514 super dust storm. We further investigated the  $[\text{NH}_4^++\text{Ca}^{2+}+\text{Mg}^{2+}]/[\text{SO}_4^{2-}+\text{NO}_3^-]$  ratio.  
515 As shown in Fig. 7d, with the addition of  $\text{Ca}^{2+}$  and  $\text{Mg}^{2+}$ , sulfate and nitrate had been  
516 completely neutralized, implying the important role of alkaline calcium and  
517 magnesium as the medium of dust heterogeneous reactions. By estimating the  
518 neutralization efficiency of  $\text{Ca}^{2+}$  and  $\text{Mg}^{2+}$  ( $\text{NE}_{\text{Ca}\&\text{Mg}}$ ) as  $\text{NE}_{\text{Ca}\&\text{Mg}} = 1 -$   
519  $[\text{NH}_4^+]/[\text{SO}_4^{2-}+\text{NO}_3^-]$ , the average value of  $\text{NE}_{\text{Ca}\&\text{Mg}}$  in DS1 and DS2 was 0.34 and  
520 0.50, respectively. The higher  $\text{NE}_{\text{Ca}\&\text{Mg}}$  in DS2 also suggested the chemical  
521 processing via dust was efficient under the environmental conditions such as DS2 in  
522 this study.

523

### 524 3.5. Vertical evolution of dust particles

525 In both DS1 and DS2, dust particles were mostly refrained below the altitude of  
526 1km. Strong vertical gradients of  $\delta v$  and  $\beta$  were observed (Fig. 3). To quantitatively  
527 investigate the evolution of vertical dust profiles, we selected four typical episodes as  
528 follows: 1. 9:00-15:00 LST of March 20: an episode right before the arrival of DS1; 2.  
529 16:00 - 17:45 LST of March 20: an episode before the onset of maximum hourly  
530  $\text{PM}_{10}$  concentrations in DS1; 3. 18:00 LST of March 20 - 4:45 LST of March 21, an  
531 episode that covers the highest  $\text{PM}_{10}$  concentrations hours ( $>1000\mu\text{g}\text{m}^{-3}$ ) in DS1; 4.  
532 6:00 - 18:00 LST of March 22: an episode in DS2.

533 As shown in Fig. 8a, the mean  $\sigma$  between 9:00 - 15:00LST, March 20 ranged from  
534 around 0.12 to 0.72  $\text{km}^{-1}$  from near ground level to 1km. During this period, the mean  
535  $\delta_p$  was relatively low of  $\sim 0.02 - 0.08$ , suggesting spherical particles, i.e. pollution  
536 particles dominated. Accordingly, the contribution of dust to the total particle  
537 extinction (dust ratio) was less than 20% (Fig. 8e). As discussed earlier, the high  
538 values of light extinction caused by pollution particles before the onset of DS1 were  
539 due to the pre-accumulation of local and transported pollutants brought by the invaded  
540 cold front. On the pathway of DS1 (Fig. 2c), the air masses travelled over large areas  
541 with intense anthropogenic emissions and thus a large quantity of pollutants could be  
542 pushed to the downstream areas and accumulated before the dust plume arrived.

543 As DS1 invaded, the mean  $\sigma$  further increased and reached 0.73  $\text{km}^{-1}$  near the  
544 surface level (Fig. 8b-c). In the meantime, the values of  $\delta_p$  were elevated to be higher  
545 than 10% from near the ground to  $\sim 1\text{km}$  (Fig.8f-g). When  $\text{PM}_{10}$  reached its highest  
546 concentrations ( $>1000\mu\text{g}\text{m}^{-3}$ ), the mean  $\delta_p$  was  $\sim 23\text{-}27\%$  extending from near the  
547 ground to  $\sim 700\text{m}$  (Fig.8g). However, compared to the  $\delta_p$  value of  $\sim 30\text{-}35\%$  for the  
548 relatively pure Asian dust (Murayama et al., 2003; Sakai et al., 2003), the  $\delta_p$  in DS1  
549 was still lower, suggesting the mixing of dust with pollution at a certain extent. As  
550 shown in Fig. 8b-c, the mean  $\sigma_d$  obviously overwhelmed the mean  $\sigma_s$  and could be up  
551 to 0.82  $\text{km}^{-1}$  near the surface level, while the mean  $\sigma_s$  dropped to less than 0.1  $\text{km}^{-1}$ .  
552 From near the ground to  $\sim 700\text{m}$ , no significant vertical gradients of  $\delta_p$  and dust ratio  
553 were observed. This indicated DS1 had a “top-down” effect on modifying the bulk  
554 particle optical properties in the lower troposphere in this case. Within this altitude  
555 range, dust could account for  $\sim 80 - 90\%$  of the total particle extinction coefficients  
556 while only a minor fraction of  $\sim 10 - 20\%$  was attributed to the pollution particles.  
557 Above 700m,  $\delta_p$  and the dust ratio quickly decreased, suggesting the impact of dust on  
558 the light extinction was much weakened.

559 In DS2, the maximum  $\sigma$  and  $\delta_p$  averaged between 6:00 and 18:00 LST, March 22  
560 was  $\sim 0.61\text{km}^{-1}$  and 26%, respectively, observed at an altitude of  $\sim 300\text{m}$ . Different

561 from DS1, both  $\delta p$  and the dust ratio had a significant vertical gradient in DS2. As  
562 showed in Fig. 8h,  $\delta p$  decreased quickly from its maximum value at  $\sim 250\text{m}$  to 5% at  
563  $\sim 750\text{m}$ . Correspondingly, the dust ratios decreased from 88% to 25%. Moreover, the  
564 vertical profiles of  $\sigma_d$  and  $\sigma_s$  showed distinctly different behaviors during this period.  
565 As shown in Fig. 8d, the maximum  $\sigma_d$  ( $\sim 0.55 \text{ km}^{-1}$ ) showed at the altitude of  $\sim 250\text{m}$ ,  
566 while that of  $\sigma_s$  ( $\sim 0.25 \text{ km}^{-1}$ ) appeared at a higher altitude of  $\sim 800\text{m}$ . As compared to  
567 DS1 (Fig. 8b-c), the  $\sigma_s$  in DS2 showed similar magnitudes below  $\sim 270\text{m}$ . Above this  
568 altitude, the  $\sigma_s$  in DS2 gradually increased while that in DS1 varied relatively stable  
569 with the altitudes. The enhancement of pollution particles in the middle layer during  
570 DS2 should be mainly attributed to its unique transport pathway. As shown in Fig. 2e,  
571 substantial air masses in the upper layer transported from the south and may bring  
572 more moisture. The sounding data at a meteorology station ( $31.40^\circ\text{N}$ ,  $121.46^\circ\text{E}$ ) in  
573 Shanghai supported this statement as shown in Fig. S2.

574 Opposite to the low relative humidity (RH) and its decreasing trend with altitude in  
575 DS1, RH in DS2 (measured at 8:00 and 20:00 LST of March 22, respectively) showed  
576 much higher values and an increasing trend with altitude (Fig. S2). This phenomenon  
577 corroborated our discussions above that the meteorological conditions were more  
578 favorable for promoting the dust chemistry in DS2. As a result, the secondary aerosol  
579 formation via heterogeneous reaction yielded stronger particle extinction in DS2,  
580 especially in the middle and upper layers through 270m till the top (2km) where the  
581 particle extinctions caused by spherical particles were still significant. On the other  
582 hand, due to the higher humidity in DS2, the soluble particle components should  
583 undergo stronger hygroscopic growth and thus partly explain the structure of vertical  
584 profile of spherical particles as shown in Fig. 8d. It is commonly regarded that in a  
585 dry and less oxidative environment that dust storms are usually associated with, the  
586 formation and growth of secondary particles are often depressed. However, under  
587 certain favorable conditions, new particle formation during dust events could be still  
588 discernible (Nie et al., 2014). In this study, vertical profiles of crucial meteorological

589 parameters, pollutant precursors and particle numbers were not available for  
590 diagnosing the new particle formation. Tethered balloon-based measurement (Li et al.,  
591 2015) could be a good platform for investigating the particle formation during dust  
592 events at different altitudes in the future research.

593

### 594 **3.6 Impact of dust chemistry on regional air quality**

595 Chemical transport modeling (Methods in Section 2.5) was utilized to assess the  
596 impact of dust chemistry on the perturbation of air quality at the regional scale. The  
597 model performance of CMAQ with improved dust module has been evaluated against  
598 various observational datasets and it was demonstrated that the model has relatively  
599 good capability in capturing both magnitudes and temporal variability of bulk aerosol  
600 (e.g. PM<sub>10</sub>, AOD) during the spring season over China (Dong et al., 2016). It has to be  
601 noted that the model only simulated the **particle** size up to 10 μm while the  
602 observation of **particle** chemistry included all the sizes (i.e. TSP), hence the mismatch  
603 of size distribution between the model and observation precluded the evaluation of the  
604 simulated **particle** chemical species in this study. In the following discussions, we  
605 focused on the qualitative assessment of the impact of dust chemistry on the regional  
606 air quality.

607 Fig. 9 shows the spatial distribution of simulated mineral **particles** from March 20 –  
608 22, 2010, respectively. Accordingly, we show the spatial distribution of Ultraviolet  
609 Aerosol Index (UVAI) retrieved from OMI during the same period. UVAI is sensitive  
610 to absorbing **particles**, i.e. black carbon and mineral dust (Torres et al., 2007). Hence,  
611 the comparison between simulated mineral **particles** and observed UVAI could  
612 illustrate how the transport of dust was reproduced. **However, based on the definition**  
613 **of Aerosol Index, it is a parameter based on the difference between radiance at two**  
614 **near ultraviolet wavelengths. Thus, the comparison between satellite Aerosol Index**  
615 **and simulated mineral dust is only qualitative.** As seen from Fig. 9, high values of  
616 UVAI were always observed over the Indo-China Peninsula and this was ascribed to

617 the black carbon particles emitted from strong biomass burning over this region  
618 during the spring season (Fu et al., 2012; Huang et al., 2013; Tsay et al., 2013). What  
619 we concern are the dust and its downwind regions over East Asia. On March 20, high  
620 UVAI values stretched from the Gobi Desert to the North China Plain and the Yangtze  
621 River Delta. This transport pathway was relatively well reproduced by the model as  
622 we can see high concentrations of mineral particles over similar areas as well. On the  
623 following day of March 21, the satellite observation illustrated the movement of the  
624 high UVAI zones further southward and the drifting of dust plumes off the coastline  
625 of East China (Fig. 9c). Accordingly, the simulation showed similar behavior with  
626 strengthened concentrations of mineral particles over the Gobi Desert and downwind  
627 areas of the Yangtze River Delta (Fig. 9d). On March 22, although UVAI signals were  
628 absent over most areas of East China due to the satellite swath, high UVAI values  
629 could still be observed over the tip of the Yangtze River Delta and the East China Sea.  
630 This is also relatively consistent with the model simulation that high concentrations of  
631 mineral particles hovered over the coastlines from YRD to the Taiwan Strait. Overall,  
632 we demonstrated that the model is capable of capturing the spatial distribution of dust  
633 during the long-range transport.

634 Since we specifically focus on the interaction between dust and anthropogenic  
635 pollutants in this study, we have performed two simulations, i.e. one with dust  
636 emissions but without dust chemistry and the other one with dust chemistry. The  
637 impact of dust chemistry on particle chemical components could thus be quantified  
638 via the difference between these two simulations. Fig. 10a&c shows the spatial  
639 distribution of sulfate via the formation pathway of dust heterogeneous reactions, as  
640 well as for nitrate in Fig. 10b&d. Different from the spatial distribution of mineral  
641 particles (Fig. 9a-c), the formation of sulfate and nitrate via dust chemistry mainly  
642 occurred over Northeastern China. This is expected that although the major source  
643 region of mineral dust is from the Gobi Desert in Northern China, less anthropogenic  
644 emission sources existed there, hence relatively weak atmospheric chemical



645 processing was simulated over the dust source region. On the other hand, drier climate  
646 in Northern China also suppressed the extent of heterogeneous reactions on the  
647 surface of dust. Hence, the strongest impact from dust heterogeneous reactions on the  
648 formation of secondary **particles** occurred in those populous areas where the  
649 interaction of anthropogenic precursors and dust was the strongest.

650 As for sulfate, the simulated concentration over Shanghai averaged 8.1, 3.1, and 8.5  
651  $\mu\text{gm}^{-3}$  from March 20 – 22, respectively. This temporal variation corresponded to that  
652 from observation as discussed in Section 3.4.2. While it has to be noted again that the  
653 simulated **particle** species contained particulate sizes less than 10  $\mu\text{m}$ , close match  
654 between the simulation and observation was not expected. As we compare DS1 (Fig.  
655 10a) and DS2 (Fig. 10c), the simulated sulfate during DS2 was evidently more intense  
656 than that during DS1 at a larger geographic region, which was fairly consistent with  
657 the observation. Since the daily emission rates digested by the model were almost  
658 constant during this period, meteorological conditions should be the determining  
659 factor, of which elevated humidity during DS2 has been diagnosed as the most  
660 important factor responsible for stronger dust chemistry.

661 As for nitrate, its spatial distribution pattern was as similar as that of sulfate at a  
662 certain extent. The simulated concentration of nitrate averaged 3.1, 2.3, and 5.2  $\mu\text{gm}^{-3}$   
663 over Shanghai from March 20 – 22, respectively. Although the simulation results and  
664 observational data couldn't be statistically inter-compared due to the size difference as  
665 stated above, we think the simulated nitrate should be largely underestimated. The  
666 ratio of simulated nitrate between DS2 and DS1 was 1.7, similar to that of  $\sim 1.6$  from  
667 observation. This suggested the favorable meteorological conditions (e.g. higher  
668 humidity) on facilitating the dust heterogeneous reaction during DS2 have been  
669 accounted by the model. In this regard, we ascribe the low- biased nitrate mainly to  
670 several aspects. First, the  $\text{NO}_x$  emissions could have been underestimated. As  
671 indicated in Dong et al. (2015) which used the same anthropogenic emission  
672 inventory as this study, the model showed some underestimation of the total  $\text{NO}_2$



673 columns as compared to the OMI observation, especially over Northeastern China  
674 (See Fig. 8 in Dong et al.(2015)). Secondly, HNO<sub>3</sub>, N<sub>2</sub>O<sub>5</sub>, NO<sub>2</sub> and NO<sub>3</sub> were the  
675 major precursors of nitrate as implemented in the dust module. Of which, reactions  
676 via HNO<sub>3</sub> and N<sub>2</sub>O<sub>5</sub> were the dominant pathways of nitrate formation due to their  
677 relatively high uptake coefficients on the dust. It was possible that the formation of  
678 HNO<sub>3</sub> was underestimated, thus lowering the production of nitrate. However, this is  
679 just a guess as observation of gaseous HNO<sub>3</sub> was not available in this study. Lastly,  
680 we think the underestimation of nitrate may be due to the omission of nitrate  
681 processing on the surface of sea salt, which was especially important for costal cities  
682 such as Shanghai (Buseck and Posfai, 1999).

683  
684

#### 685 **4. Conclusions**

686 During March 19-23, 2010, a super dust storm swept extensive areas over China  
687 from Northern China to Southern China. Two separate dust periods were observed in  
688 Shanghai, one from ~16:00 LST, March 20 to ~10:00 LST March 21 (DS1) and the  
689 other from ~6:00 LST, March 22 to ~0:00 LST, March 23 (DS2). In DS1, the dust  
690 plumes mostly transported over those areas characterized of high pollution emissions  
691 in Northern China, while the dust plumes in DS2 transported over the coastal regions  
692 of Eastern China with higher RH. The ratios of SO<sub>2</sub>/PM<sub>10</sub> and NO<sub>2</sub>/PM<sub>10</sub> were up to  
693  $0.11 \pm 0.03$  and  $0.20 \pm 0.04$  in DS2, much higher than the values in DS1. In addition,  
694 the concentrations of typical elemental species such as As, Cd, Pb, and Zn were also  
695 more enriched in DS2 than in DS1, indicating the stronger mixing extent between dust  
696 and primary anthropogenic emissions in DS2. Due to the higher level of gaseous  
697 pollutant precursors associated with moderate relative humidity, SO<sub>4</sub><sup>2-</sup> and NO<sub>3</sub><sup>-</sup>  
698 exhibited higher concentrations in DS2 than in DS1. The higher Ca<sup>2+</sup>/Ca ratio and  
699 lower [NH<sub>4</sub><sup>+</sup>]/[SO<sub>4</sub><sup>2-</sup>+NO<sub>3</sub><sup>-</sup>] ratio in DS2 suggested the heterogeneous reactions  
700 between calcites and acid gases were significantly promoted in DS2. Particularly,  
701 more NO<sub>3</sub><sup>-</sup> than SO<sub>4</sub><sup>2-</sup> was formed in DS2, probably due to the high concentrations of

702 NO<sub>2</sub> and the complex reaction among dust, seasalts, and nitric acid. Vertical profiles  
703 of **particle** optical properties from Lidar measurement retrieved high depolarization  
704 ratios of 20-25% extending from near the ground to ~700m in DS1 and it was  
705 estimated that dust dominantly accounted for ~80-90% of the total **particle** extinction.  
706 In DS2, the vertical structure of **particles** changed dramatically from that of DS1. The  
707 maximum extinction coefficient of dust particles emerged at the altitude of ~250m in  
708 DS2, while that of pollution particles showed at a higher altitude of ~800m. The  
709 abnormal increase of humidity as a function of altitude from the southerly winds  
710 explained this phenomenon due to promoted heterogeneous reactions on dust particles  
711 and the subsequent **particle** hygroscopic growth.

712 Simulated mineral **particles** were compared to the remote sensing UVAI from  
713 satellite, showing consistent spatial patterns between model and observation. By  
714 applying the dust scheme with explicit chemistry mechanisms, evident impacts of dust  
715 heterogeneous reactions on secondary aerosol formation were reproduced over  
716 widespread areas of Northeastern China where the anthropogenic emissions were  
717 intensive. The sulfate formation was relatively well simulated while the nitrate  
718 formation on dust was believed to be largely underestimated. More research on  
719 laboratory kinetic studies of nitrate dust chemistry is suggested. Also, the feedback  
720 between dust chemistry and regional climate change needs to be investigated in the  
721 future.

722

## 723 **Acknowledgment**

724 This work was supported by the National Natural Science Foundation of China  
725 (Nos. 41405115, 41429501, and 91644105) and National Key Technology Research  
726 and Development Program of the Ministry of Science and Technology of China (No.  
727 2014BAC22B06). Dr. Qingyan Fu and Yanfen Lin would like to acknowledge support  
728 from Shanghai Science and Technology Fund (Nos. 14DZ1202900 and 16DZ1204601)  
729 and National Key Technology Research and Development Program of the Ministry of

730 Science and Technology of China (No. 2014BAC22B00).

731

732 **References:**

733 Bi, J., Huang, J., Holben, B., 2016. Comparison of key absorption and optical  
734 properties between pure and transported anthropogenic dust over East and Central  
735 Asia. 1-37.

736 Bi, J., Shi, J., Xie, Y., 2014. Dust Aerosol Characteristics and Shortwave Radiative  
737 Impact at a Gobi Desert of Northwest China during the Spring of 2012. *Journal of the*  
738 *Meteorological Society of Japan* 92, 33-56.

739 Buseck, P., Posfai, M., 1999. Airborne minerals and related aerosol particles: Effects  
740 on climate and the environment. *Proc. Natl. Acad. Sci. U. S. A.*, 3372–3379, doi:  
741 10.1073/pnas.96.7.3372.

742 Chen S., J. Huang, L. Kang, H. Wang, X. Ma, Y. He, T. Yuan, B. Yang, Z. Huang,  
743 and G. Zhang (2017). Emission, transport and radiative effects of mineral dust from  
744 Taklimakan and Gobi Deserts: comparison of measurements and model results.  
745 *Atmospheric Chemistry and Physics*,17(3):1-43, doi: 10.5194/acp-17-2401-2017.

746 Creamean, J.M., Suski, K.J., Rosenfeld, D., Cazorla, A., Demott, P.J., Sullivan, R.C.,  
747 White, A.B., Ralph, F.M., Minnis, P., Comstock, J.M., 2013. Dust and biological  
748 aerosols from the Sahara and Asia influence precipitation in the western U.S. *Science*  
749 339, 1572.

750 Dong, X., Fu, J.S., Huang, K., Tong, D., Zhuang, G., 2015. Model development of  
751 dust emission and heterogeneous chemistry within the Community Multiscale Air  
752 Quality modeling system and its application over East Asia. *Atmospheric Chemistry*  
753 *& Physics* 15, 35591-35643.

754 Dupart, Y., King, S.M., Nekat, B., Nowak, A., Wiedensohler, A., Herrmann, H., David,  
755 G., Thomas, B., Miffre, A., Rairoux, P., 2012. Mineral dust photochemistry induces  
756 nucleation events in the presence of SO<sub>2</sub>. *Proc Natl Acad Sci U S A* 109,  
757 20842-20847.

758 Duvall, R.M., Majestic, B.J., Shafer, M.M., Chuang, P.Y., Simoneit, B.R.T., Schauer,  
759 J.J., 2008. The water-soluble fraction of carbon, sulfur, and crustal elements in Asian  
760 aerosols and Asian soils. *Atmospheric Environment* 42, 5872-5884.

761 Eguchi, K., I. Uno, K. Yumimoto, et al., 2009: Trans-pacific dust transport: integrated  
762 analysis of NASA/CALIPSO and a global aerosol transport model. *Atmos. Chem.*  
763 *Phys.*, 9, 3137-3145.

764 Fernald, F.G., 1984. Analysis of atmospheric lidar observations: some comments.  
765 *Applied Optics* 23, 652.

766 Fischer, E.V., Perry, K.D., Jaffe, D.A., 2011. Optical and chemical properties of  
767 aerosols transported to Mount Bachelor during spring 2010. *Journal of Geophysical*  
768 *Research-Atmospheres* 116, 13.

769 Formenti, P., Schutz, L., Balkanski, Y., Desboeufs, K., Ebert, M., Kandler, K., Petzold,  
770 A., Scheuven, D., Weinbruch, S., Zhang, D., 2011. Recent progress in understanding

771 physical and chemical properties of African and Asian mineral dust. *Atmospheric*  
772 *Chemistry and Physics* 11, 8231-8256.

773 Fu, J.S., Hsu, N.C., Gao, Y., Huang, K., Li, C., Lin, N.H., Tsay, S.C., 2012. Evaluating  
774 the influences of biomass burning during 2006 BASE-ASIA: a regional chemical  
775 transport modeling. *Atmospheric Chemistry & Physics* 12, 5271-5273.

776 Fu, Q.Y., Zhuang, G.S., Li, J.A., Huang, K., Wang, Q.Z., Zhang, R., Fu, J., Lu, T.,  
777 Chen, M., Wang, Q.A., Chen, Y., Xu, C., Hou, B., 2010. Source, long-range transport,  
778 and characteristics of a heavy dust pollution event in Shanghai. *Journal of*  
779 *Geophysical Research-Atmospheres* 115, -.

780 Fu, X., S. X. Wang, Z. Cheng, J. Xing, B. Zhao, J. D. Wang, and J. M. Hao, 2014:  
781 Source, transport and impacts of a heavy dust event in the Yangtze River Delta, China,  
782 in 2011. *Atmos. Chem. Phys.*, 14, 1239–1254.

783 Guenther, A., Karl, T., Harley, P., Wiedinmyer, C., Palmer, P.I., Geron, C., 2006.  
784 Estimates of global terrestrial isoprene emissions using MEGAN (Model of Emissions  
785 of Gases and Aerosols from Nature). *Atmospheric Chemistry & Physics* 6, 3181-3210.

786 Guo, J., Rahn, K.A., Zhuang, G.S., 2004. A mechanism for the increase of pollution  
787 elements in dust storms in Beijing. *Atmospheric Environment* 38, 855-862.

788 Hsu, S.-C., Lee, C.S.L., Huh, C.-A., Shaheen, R., Lin, F.-J., Liu, S.C., Liang, M.-C.,  
789 Tao, J., 2014. Ammonium deficiency caused by heterogeneous reactions during a  
790 super Asian dust episode. *Journal of Geophysical Research: Atmospheres* 119,  
791 2013JD021096.

792 Huang J., T. Wang, W. Wang, Z. Li, and H. Yan, 2014: Climate effects of dust  
793 aerosols over East Asian arid and semiarid regions. *J. Geophys. Res.: Atmospheres*,  
794 119, 11398-11416.

795 Huang, K., Fu, J.S., Hsu, N.C., Gao, Y., Dong, X., Tsay, S.C., Yun, F.L., 2013. Impact  
796 assessment of biomass burning on air quality in Southeast and East Asia during  
797 BASE-ASIA. *Atmospheric Environment* 78, 291-302.

798 Huang, K., Zhuang, G., Lin, Y., Fu, J.S., Wang, Q., Liu, T., Zhang, R., Jiang, Y., Deng,  
799 C., Fu, Q., Hsu, N.C., Cao, B., 2012. Typical types and formation mechanisms of haze  
800 in an Eastern Asia megacity, Shanghai. *Atmos. Chem. Phys.* 12, 105-124.

801 Huang, K., Zhuang, G.S., Li, J.A., Wang, Q.Z., Sun, Y.L., Lin, Y.F., Fu, J.S., 2010a.  
802 Mixing of Asian dust with pollution aerosol and the transformation of aerosol  
803 components during the dust storm over China in spring 2007. *Journal of Geophysical*  
804 *Research-Atmospheres* 115, -.

805 Huang, K., Zhuang, G.S., Lin, Y.F., Li, J.A., Sun, Y.L., Zhang, W.J., Fu, J.S., 2010b.  
806 Relation between optical and chemical properties of dust aerosol over Beijing, China.  
807 *Journal of Geophysical Research-Atmospheres* 115, -.

808 IPCC, 2013. *Climate Change 2013: The Physical Science Basis*, Contribution of  
809 Working Group I to the Fifth Assessment Report of the Intergovernmental Panel on  
810 Climate Change. Cambridge University Press, New York, USA.

811 Li, J., Fu, Q., Huo, J., Wang, D., Yang, W., Bian, Q., Duan, Y., Zhang, Y., Pan, J., Lin,  
812 Y., Huang, K., Bai, Z., Wang, S.-H., Fu, J.S., Louie, P.K.K., 2015. Tethered

813 balloon-based black carbon profiles within the lower troposphere of Shanghai in the  
814 2013 East China smog. *Atmospheric Environment* 123, Part B, 327-338.

815 Li, J.W., Han, Z.W., Zhang, R.J., 2011. Model study of atmospheric particulates  
816 during dust storm period in March 2010 over East Asia. *Atmospheric Environment* 45,  
817 3954-3964.

818 Li, R., Min, Q.L., 2010. Impacts of mineral dust on the vertical structure of  
819 precipitation. *Journal of Geophysical Research-Atmospheres* 115, 14.

820 Lida, D.R., 2006. *Handbook of Chemistry and Physics: A Ready-Reference Book of*  
821 *Chemical and Physical Data*. 86th ed. CRC Press, New York, 14-17.

822 Liu, Z.Y., Sugimoto, N., Murayama, T., 2002. Extinction-to-backscatter ratio of Asian  
823 dust observed with high-spectral-resolution lidar and Raman lidar. *Applied Optics* 41,  
824 2760-2767.

825 Matsuki, A., Iwasaka, Y., Shi, G., Zhang, D., Trochkin, D., Yamada, M., Kim, Y.S.,  
826 Chen, B., Nagatani, T., Miyazawa, T., 2006. Morphological and chemical  
827 modification of mineral dust: Observational insight into the heterogeneous uptake of  
828 acidic gases. *Geophysical Research Letters* 32, 312-329.

829 Murayama, T., Masonis, S.J., Redemann, J., Anderson, T.L., Schmid, B., Livingston,  
830 J.M., Russell, P.B., Huebert, B., Howell, S.G., McNaughton, C.S., 2003. An  
831 intercomparison of lidar-derived aerosol optical properties with airborne  
832 measurements near Tokyo during ACE-Asia. *Journal of Geophysical Research*  
833 *Atmospheres* 108, 8561.

834 Nie, W., Ding, A., Wang, T., Kerminen, V.-M., George, C., Xue, L., Wang, W., Zhang,  
835 Q., Petäjä, T., Qi, X., Gao, X., Wang, X., Yang, X., Fu, C., Kulmala, M., 2014.  
836 Polluted dust promotes new particle formation and growth. *Scientific Reports*, 4(2),  
837 6634.

838 Pan, X., Uno, I., Zhe, W., Nishizawa, T., Sugimoto, N., Yamamoto, S., Yamamoto, S.,  
839 Kobayashi, H., Sun, Y., Fu, P., Tang, X., and Wang Z., 2017. Real-time observational  
840 evidence of changing asian dust morphology with the mixing of heavy anthropogenic  
841 pollution. *Scientific Reports*, 7(1), 335.

842 Reid, J.S., Hyer, E.J., Prins, E.M., Westphal, D.L., Zhang, J., Wang, J., Christopher,  
843 S.A., Curtis, C.A., Schmidt, C.C., Eleuterio, D.P., 2009. Global Monitoring and  
844 Forecasting of Biomass-Burning Smoke: Description of and Lessons From the Fire  
845 Locating and Modeling of Burning Emissions (FLAMBE) Program. *IEEE Journal of*  
846 *Selected Topics in Applied Earth Observations & Remote Sensing* 2, 144-162.

847 Sakai, T., Nagai T., Nakazato M., Mano Y., and Matsumura T., 2003. Ice clouds and  
848 Asian dust studied with lidar measurements of particle extinction-to-backscatter ratio,  
849 particle depolarization, and water-vapor mixing ratio over Tsukuba, *Applied Optics* 42,  
850 7103–7116.

851 Shimizu, A., Sugimoto, N., Matsui, I., Arao, K., Uno, I., Murayama, T., Kagawa, N.,  
852 Aoki, K., Uchiyama, A., Yamazaki, A., 2004. Continuous observations of Asian dust  
853 and other aerosols by polarization lidars in China and Japan during ACE-Asia. *Journal*  
854 *of Geophysical Research: Atmospheres* 109, D19S17.

855 Shimizu, A., Nishizawa, T., Jin, Y., Kim, S. W., Wang, Z., Batdorj, D., Sugimoto, N.,  
856 2017. Evolution of a lidar network for tropospheric aerosol detection in east asia.  
857 *Optical Engineering*, 56(3), 031219.

858 Sugimoto, N., Matsui, I., Shimizu, A., Uno, I., Asai, K., Endoh, T., Nakajima, T., 2002.  
859 Observation of dust and anthropogenic aerosol plumes in the Northwest Pacific with a  
860 two-wavelength polarization lidar on board the research vessel Mirai. *Geophysical*  
861 *Research Letters* 29.

862 Sullivan, R.C., Guazzotti, S.A., Sodeman, D.A., Prather, K.A., 2007. Direct  
863 observations of the atmospheric processing of Asian mineral dust. *Atmospheric*  
864 *Chemistry & Physics* 7, 1213-1236.

865 Sun, Y.L., Jiang, Q., Wang, Z.F., Fu, P.Q., Li, J., Yang, T., Yin, Y., 2014. Investigation  
866 of the sources and evolution processes of severe haze pollution in Beijing in January  
867 2013. *J Geophys Res-Atmos* 119, 4380-4398.

868 Sun, Y.L., Zhuang, G.S., Huang, K., Li, J.A., Wang, Q.Z., Wang, Y., Lin, Y.F., Fu, J.S.,  
869 Zhang, W.J., Tang, A.H., Zhao, X.J., 2010. Asian dust over northern China and its  
870 impact on the downstream aerosol chemistry in 2004. *Journal of Geophysical*  
871 *Research-Atmospheres* 115, -.

872 Sun, Y.L., Zhuang, G.S., Ying, W., Han, L.H., Guo, J.H., Mo, D., Zhang, W.J., Wang,  
873 Z.F., Hao, Z.P., 2004. The air-borne particulate pollution in Beijing - concentration,  
874 composition, distribution and sources. *Atmospheric Environment* 38, 5991-6004.

875 Tatarov, B., Muller, D., Noh, Y.M., Lee, K.H., Shin, D.H., Shin, S.K., Sugimoto, N.,  
876 Seifert, P., Kim, Y.J., 2012. Record heavy mineral dust outbreaks over Korea in 2010:  
877 Two cases observed with multiwavelength aerosol/depolarization/Raman-quartz lidar.  
878 *Geophysical Research Letters* 39, 5.

879 Tobo, Y., Zhang, D.Z., Matsuki, A., Iwasaka, Y., 2010. Asian dust particles converted  
880 into aqueous droplets under remote marine atmospheric conditions. *Proc. Natl. Acad.*  
881 *Sci. U. S. A.* 107, 17905-17910.

882 Torres, O., Tanskanen, A., Veihelmann, B., Ahn, C., Braak, R., Bhartia, P.K., Veeffkind,  
883 P., Levelt, P., 2007. Aerosols and surface UV products from Ozone Monitoring  
884 Instrument observations: An overview. *J Geophys Res-Atmos* 112.

885 Tsai, J-H T, Huang K-L, Lin, N-H, Chen, S-J, Lin, T-Chang, Chen, S-C, Lin, C.-C.,  
886 Hsu, S.-C., Lin, W.-Y., 2012. Influence of an Asian Dust Storm and Southeast Asian  
887 Biomass Burning on the Characteristics of Seashore Atmospheric Aerosols in  
888 Southern Taiwan. *Aerosol & Air Quality Research* 12, 1105-1115.

889 Tsai, F., Tu, J.-Y., Hsu, S.-C., Chen, W.-N., 2014. Case study of the Asian dust and  
890 pollutant event in spring 2006: Source, transport, and contribution to Taiwan. *Science*  
891 *of the Total Environment* 478, 163-174.

892 Tsai, F.J., Fang, Y.S., Huang, S.J., 2013. CASE STUDY OF ASIAN DUST EVENT  
893 ON MARCH 19-25, 2010 AND ITS IMPACT ON THE MARGINAL SEA OF  
894 CHINA. *J. Mar. Sci. Technol.-Taiwan* 21, 353-360.

895 Tsay, S.C., Hsu, N.C., Lau, K.M., Li, C., Gabriel, P.M., Ji, Q., Holben, B.N., Welton,  
896 E.J., Nguyen, A.X., Janjai, S., 2013. From BASE-ASIA toward 7-SEAS: A

897 satellite-surface perspective of boreal spring biomass-burning aerosols and clouds in  
898 Southeast Asia. *Atmospheric Environment* 78, 20-34.

899 Uchiyama, A., Yamazaki, A., Togawa, H., Asano, J., Shi, G., 2005. Single Scattering  
900 Albedo of Aeolian Dust as Inferred from Sky-radiometer and in situ Ground-based  
901 Measurement. *Scientific Online Letters on the Atmosphere Sola* 1, 209-212.

902 Uno, I., Eguchi, K., Yumimoto, K., Takemura, T., Shimizu, A., Uematsu, M., Liu, Z.Y.,  
903 Wang, Z.F., Hara, Y., Sugimoto, N., 2009. Asian dust transported one full circuit  
904 around the globe. *Nature Geoscience* 2, 557-560.

905 Wang, S.-H., Hsu, N.C., Tsay, S.-C., Lin, N.-H., Sayer, A.M., Huang, S.-J., Lau,  
906 W.K.M., 2012. Can Asian dust trigger phytoplankton blooms in the oligotrophic  
907 northern South China Sea? *Geophysical Research Letters* 39, L05811.

908 Wang, S.H., Lin, N.H., OuYang, C.F., Wang, J.L., Campbell, J.R., Peng, C.M., Lee,  
909 C.T., Sheu, G.R., Tsay, S.C., 2010. Impact of Asian dust and continental pollutants on  
910 cloud chemistry observed in northern Taiwan during the experimental period of  
911 ABC/EAREX 2005. *Journal of Geophysical Research-Atmospheres* 115, -.

912 Wang, S.H., Tsay, S.C., Lin, N.H., Hsu, N.C., Bell, S.W., Li, C., Ji, Q., Jeong, M.J.,  
913 Hansell, R.A., Welton, E.J., Holben, B.N., Sheu, G.R., Chu, Y.C., Chang, S.C., Liu,  
914 J.J., Chiang, W.L., 2011. First detailed observations of long-range transported dust  
915 over the northern South China Sea. *Atmospheric Environment* 45, 4804-4808.

916 Wang, Y., Zhuang, G.S., Sun, Y., An, Z.S., 2005. Water-soluble part of the aerosol in  
917 the dust storm season - evidence of the mixing between mineral and pollution aerosols.  
918 *Atmospheric Environment* 39, 7020-7029.

919 Wang, Y., Zhuang, G.S., Sun, Y.L., An, Z.S., 2006. The variation of characteristics and  
920 formation mechanisms of aerosols in dust, haze, and clear days in Beijing.  
921 *Atmospheric Environment* 40, 6579-6591.

922 Wu, Y., Han, Z., Nazmi, C., Gross, B., Moshary, F., 2015. A trans-Pacific Asian dust  
923 episode and its impacts to air quality in the east coast of U.S. *Atmospheric*  
924 *Environment* 106, 358-368.

925 Yao, X., Chan, C.K., Fang, M., Cadle, S., Chan, T., Mulawa, P., He, K., Ye, B., 2002.  
926 The water-soluble ionic composition of PM<sub>2.5</sub> in Shanghai and Beijing, China.  
927 *Atmospheric Environment* 36, 4223-4234.

928 Yuan, H., Wang, Y., Zhuang, G., 2003. The simultaneous determination of organic  
929 acid, MSA with inorganic anions in aerosol and rainwater by ion chromatography (in  
930 Chinese). *Journal of Instrument Analysis* 6, 6-12.

931 Yuan, H., Zhuang, G.S., Li, J., Wang, Z.F., Li, J., 2008. Mixing of mineral with  
932 pollution aerosols in dust season in Beijing: Revealed by source apportionment study.  
933 *Atmospheric Environment* 42, 2141-2157.

934 Zaizen, Y., Naoe, H., Takahashi, H., Okada, K., 2014. Modification of Asian-dust  
935 particles transported by different routes – A case study. *Atmospheric Environment* 97,  
936 435-446.

937 Zhang, W.J., Zhuang, G.S., Huang, K., Li, J.A., Zhang, R., Wang, Q.Z., Sun, Y.L., Fu,  
938 J.S., Chen, Y., Xu, D.Q., Wang, W., 2010. Mixing and transformation of Asian dust

939 with pollution in the two dust storms over the northern China in 2006. Atmospheric  
940 Environment 44, 3394-3403.

941 Zhao, B., Wang, S., Dong, X., Wang, J., Duan, L., Fu, X., Hao, J., Fu, J., 2013.  
942 Environmental effects of the recent emission changes in China: implications for  
943 particulate matter pollution and soil acidification. Environmental Research Letters 8,  
944 024031.

945 Zhao, J., Zhang, F., Xu, Y., Chen, J., Yin, L., Shang, X., Xu, L., 2011. Chemical  
946 Characteristics of Particulate Matter during a Heavy Dust Episode in a Coastal City,  
947 Xiamen, 2010. Aerosol & Air Quality Research 11, 300-309.

948 Zhao, T.L., S. L. Gong, X. Y. Zhang, et al., 2006: A Simulated Climatology of Asian  
949 Dust Aerosol and Its Trans-Pacific Transport. Part I: Mean Climate and Validation. J.  
950 Climate., 19,88–103. doi: <http://dx.doi.org/10.1175/JCLI3605.1>.

951 Zhuang, G.S., Guo, J.H., Yuan, H., Zhao, X.J., 2001. The compositions, sources, and  
952 size distribution of the dust storm from China in spring of 2000 and its impact on the  
953 global environment. Chinese Science Bulletin 46, 895-901.

954 Zhuang, G.S., Yi, Z., Duce, R.A., Brown, P.R., 1992. Link between Iron and Sulfur  
955 Cycles Suggested by Detection of Fe(II) in Remote Marine Aerosols. Nature 355,  
956 537-539.



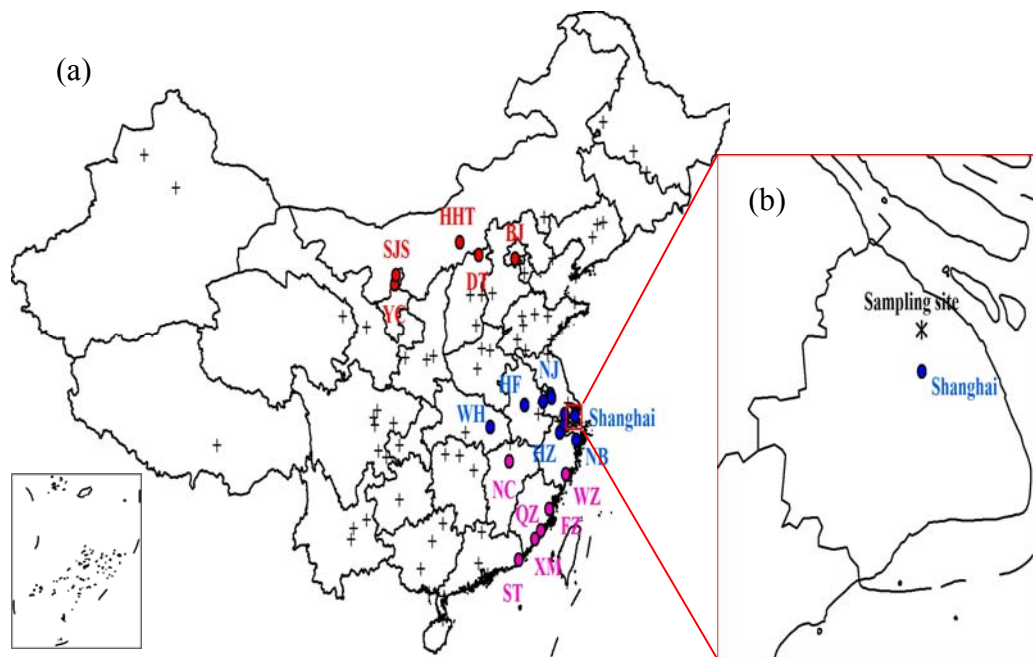
957 Table 1 Concentrations of the measured elements ( $\mu\text{g}/\text{m}^3$ ) in TSP before, during, and  
 958 after the dust periods from March 19 to 22 and in non-dust days (NDS) in Shanghai.  
 959 N, D, and NDS represent the nighttime samples collected from 20:00 to 8:00 in the  
 960 next day, the daytime samples collected from 8:00 to 20:00, and the average of the  
 961 non-dust samples collected from March 25 to 27, respectively.

962

	DS1					DS2		NDS
	19 N	20 D	20 N	21 D	21 N	22 D	22 N	
TSP	168.5	605.0	1306.7	155.1	194.3	683.3	348.2	160.5
Al	6.2	36.4	67.5	9.6	9.3	35.8	12.8	5.2
Ca	8.5	37.3	56.9	9.4	8.6	33.2	12.0	8.0
Fe	3.2	23.3	42.1	6.8	6.0	23.7	11.6	4.2
Mg	1.4	9.5	14.4	2.2	2.3	8.1	3.4	1.4
Na	1.3	7.9	19.1	2.8	3.9	7.9	3.5	2.4
Mn	0.2	1.0	2.2	0.4	0.3	1.1	0.6	0.2
Ti	0.2	1.9	4.3	0.6	0.5	1.9	0.7	0.3
Sr	$4.3 \times 10^{-2}$	$1.6 \times 10^{-1}$	$3.3 \times 10^{-1}$	$4.8 \times 10^{-2}$	$4.3 \times 10^{-2}$	$1.9 \times 10^{-1}$	$6.4 \times 10^{-2}$	$3.8 \times 10^{-2}$
V	$1.5 \times 10^{-2}$	$5.2 \times 10^{-2}$	$1.0 \times 10^{-1}$	$1.7 \times 10^{-2}$	$1.5 \times 10^{-2}$	$4.7 \times 10^{-2}$	$2.7 \times 10^{-2}$	$1.3 \times 10^{-2}$
Ni	$6.7 \times 10^{-3}$	$2.5 \times 10^{-2}$	$4.6 \times 10^{-2}$	$1.1 \times 10^{-2}$	$3.0 \times 10^{-3}$	$2.8 \times 10^{-2}$	$1.6 \times 10^{-2}$	$6.5 \times 10^{-3}$
Zn	$7.5 \times 10^{-1}$	$6.5 \times 10^{-1}$	$3.4 \times 10^{-1}$	$1.9 \times 10^{-1}$	$2.3 \times 10^{-1}$	$6.3 \times 10^{-1}$	$5.7 \times 10^{-1}$	$4.0 \times 10^{-1}$
Pb	$1.3 \times 10^{-1}$	$1.5 \times 10^{-1}$	$1.1 \times 10^{-1}$	$4.0 \times 10^{-2}$	$3.7 \times 10^{-2}$	$2.0 \times 10^{-1}$	$1.2 \times 10^{-1}$	$8.6 \times 10^{-2}$
Cu	$1.3 \times 10^{-2}$	$6.3 \times 10^{-2}$	$7.2 \times 10^{-2}$	$4.0 \times 10^{-2}$	$2.4 \times 10^{-2}$	$6.1 \times 10^{-2}$	$4.7 \times 10^{-2}$	$3.7 \times 10^{-2}$
As	$1.2 \times 10^{-2}$	$1.3 \times 10^{-2}$	$2.6 \times 10^{-2}$	$9.2 \times 10^{-3}$	$1.3 \times 10^{-2}$	$2.5 \times 10^{-2}$	$2.4 \times 10^{-2}$	$1.1 \times 10^{-2}$
Cd	$2.8 \times 10^{-3}$	$3.1 \times 10^{-3}$	$3.4 \times 10^{-3}$	$7.4 \times 10^{-4}$	$1.2 \times 10^{-3}$	$4.7 \times 10^{-3}$	$2.7 \times 10^{-3}$	$1.3 \times 10^{-3}$

963

964



965

966

967 Fig.1 (a) Locations of the 86 major cities over China. The cities with PM<sub>10</sub>

968 concentrations up to 600 $\mu\text{g}\text{m}^{-3}$  on March 20, 21, and 22 were marked by red, blue,

969 and pink circles, respectively. (b) The site location of the ground-based measurement

970 in Shanghai.

971

972

973

974

975

976

977

978

979

980

981

982

983

984

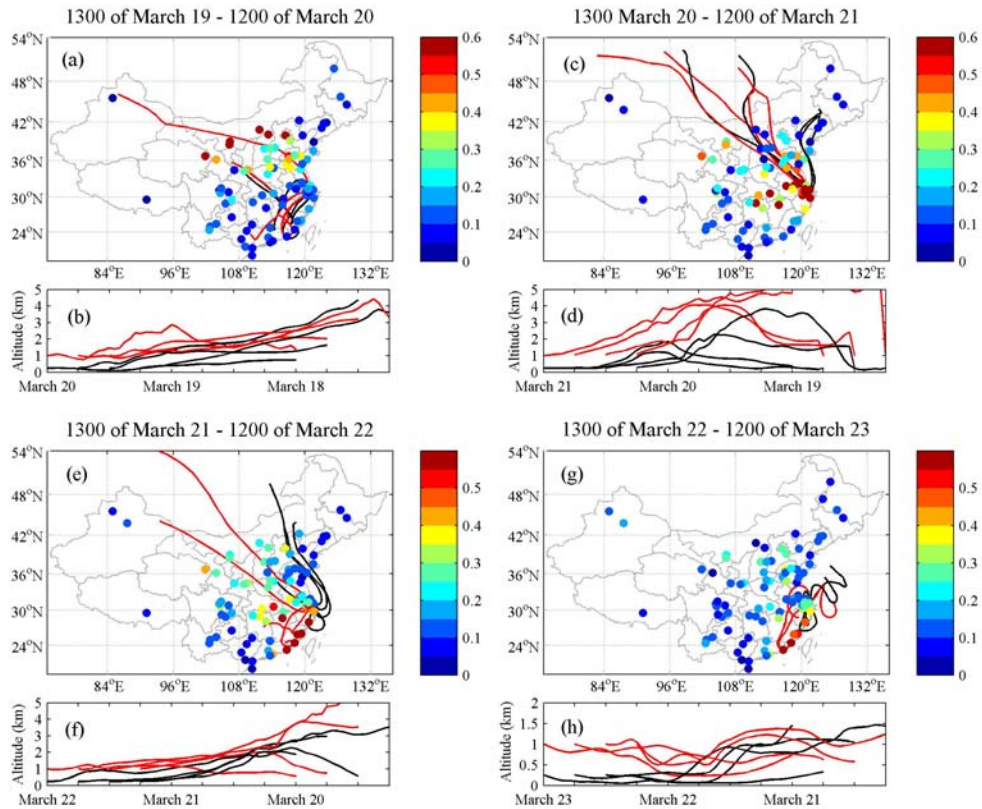
985

986

987

988

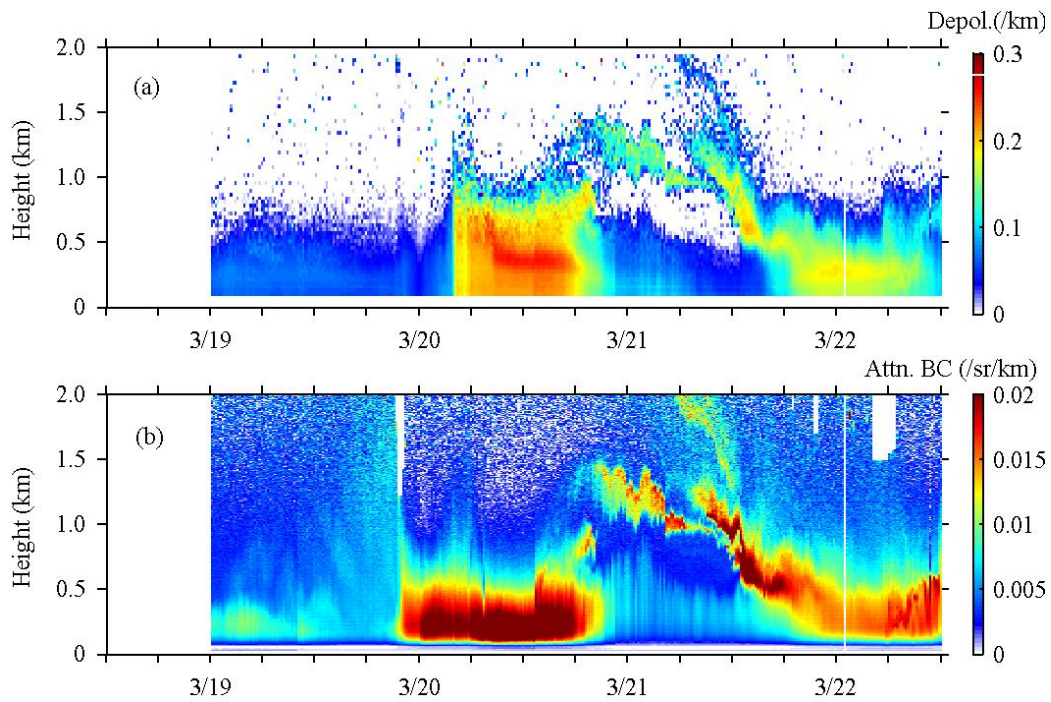
989



990  
991

992 Fig.2 Daily  $PM_{10}$  concentrations ( $mg\ m^{-3}$ ) in 86 major cities over China and 48 hours  
993 backward trajectories of the air masses at both 250m (black lines) and 1000m (red  
994 lines) above ground level over Shanghai during March 19-23, 2010. Four trajectories  
995 ending at 00, 06, 12, and 18 LST are computed for each day.

996  
997  
998  
999  
1000  
1001  
1002  
1003  
1004  
1005  
1006  
1007  
1008  
1009  
1010  
1011  
1012



1013

1014

1015

1016 Fig.3 Time-height cross-section of (a) volume depolarization ratios and (b) attenuated  
 1017 aerosol backscattering coefficients measured by a Lidar at the wavelength of 532 nm  
 1018 during March 19-22, 2010 (Local Standard Time).

1019

1020

1021

1022

1023

1024

1025

1026

1027

1028

1029

1030

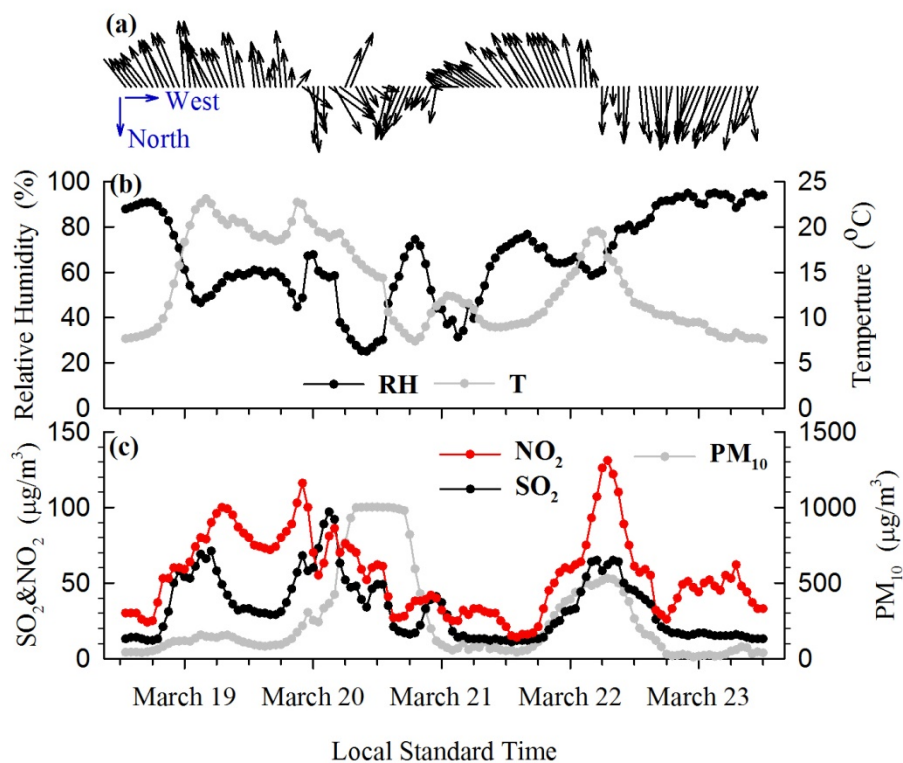
1031

1032

1033

1034

1035



1036

1037 Fig.4 Time-series of PM<sub>10</sub>, SO<sub>2</sub>, NO<sub>2</sub>, and meteorological factors including wind  
 1038 conditions, relative humidity (RH), and ambient temperature (T) in Shanghai during  
 1039 March 19-23, 2010.

1040

1041

1042

1043

1044

1045

1046

1047

1048

1049

1050

1051

1052

1053

1054

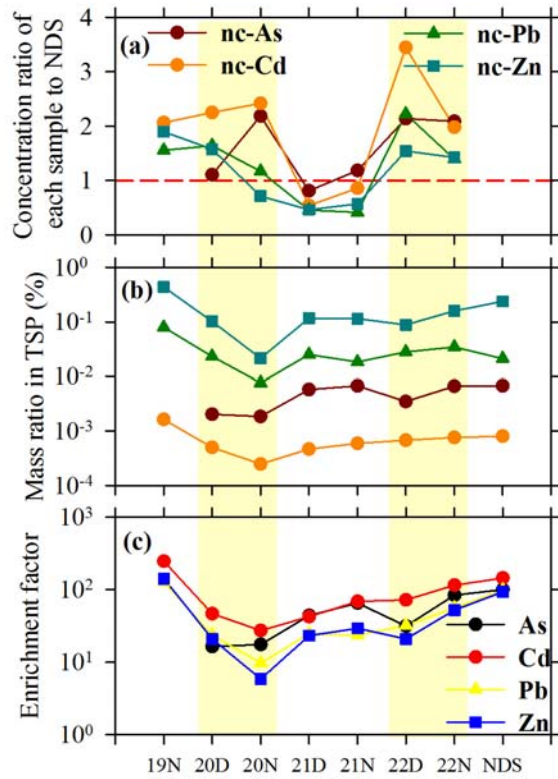
1055

1056

1057

1058

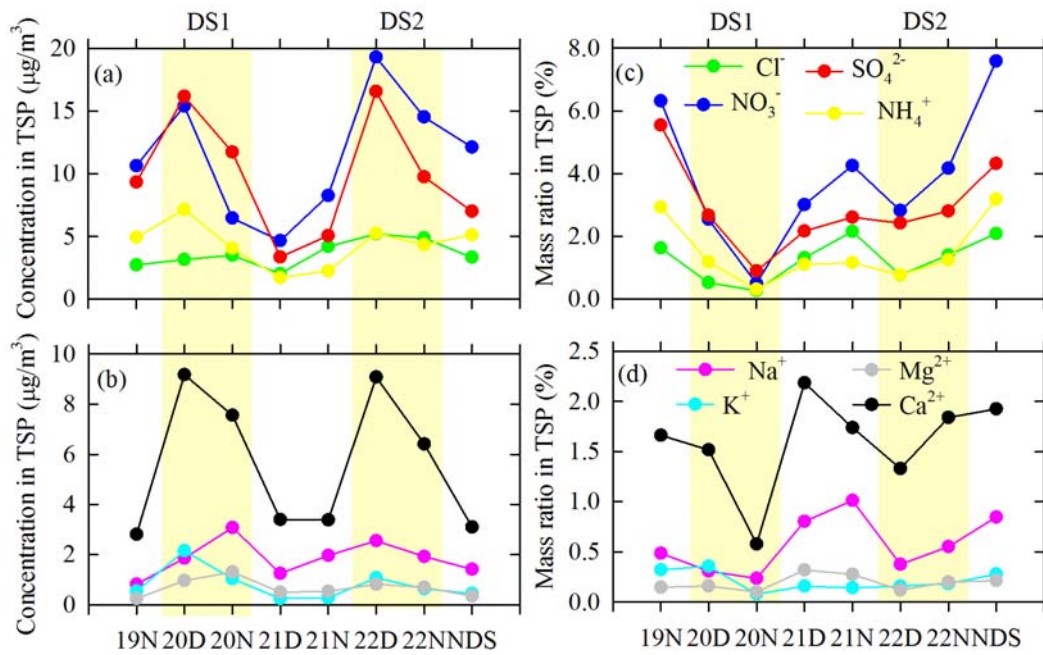
1059  
1060



1061  
1062  
1063  
1064  
1065  
1066  
1067  
1068  
1069  
1070  
1071  
1072  
1073  
1074  
1075  
1076  
1077  
1078  
1079  
1080

Fig.5 Variations of (a) the mass concentration ratio of each sample to the NDS sample for nc-As, nc-Cd, nc-Pb, and nc-Zn, (b) the mass ratios, and (c) enrichment factors of pollution elements As, Cd, Pb, and Zn in TSP during March 19-22 and non-dust days (NDS). D, N, and NDS represent the daytime samples collected from 8:00 to 20:00 LST, the nighttime samples collected from 20:00 to 8:00 LST in the next day, and the average of the non-dust samples collected from March 25 to 27, respectively.

1081  
1082

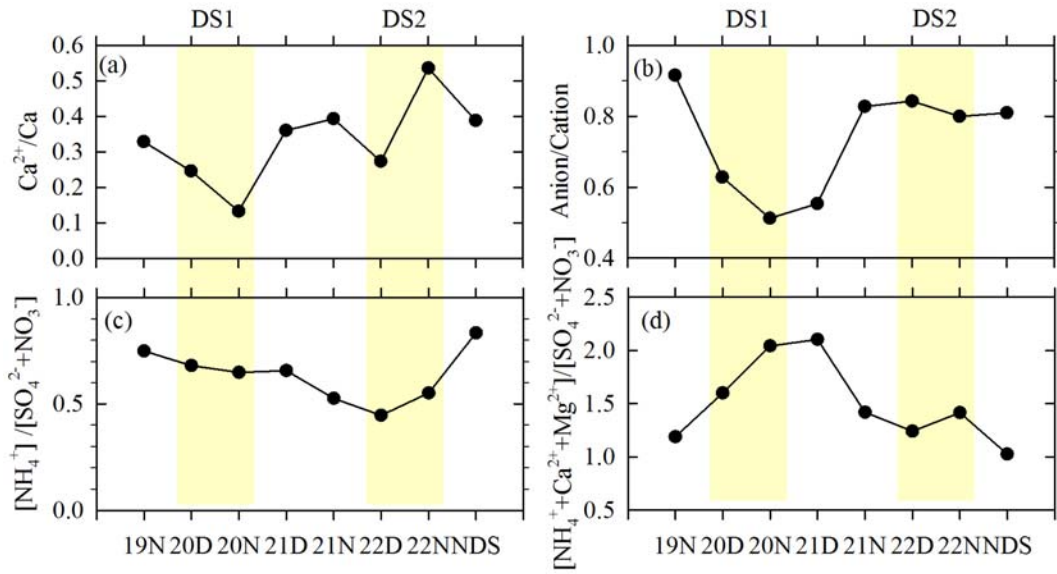


1083  
1084  
1085  
1086  
1087  
1088  
1089  
1090  
1091  
1092  
1093  
1094  
1095  
1096  
1097  
1098  
1099  
1100  
1101  
1102  
1103  
1104  
1105  
1106

Fig.6 Variations of the concentrations of water-soluble ions and their mass ratios in TSP during March 19-22 and NDS, 2010.



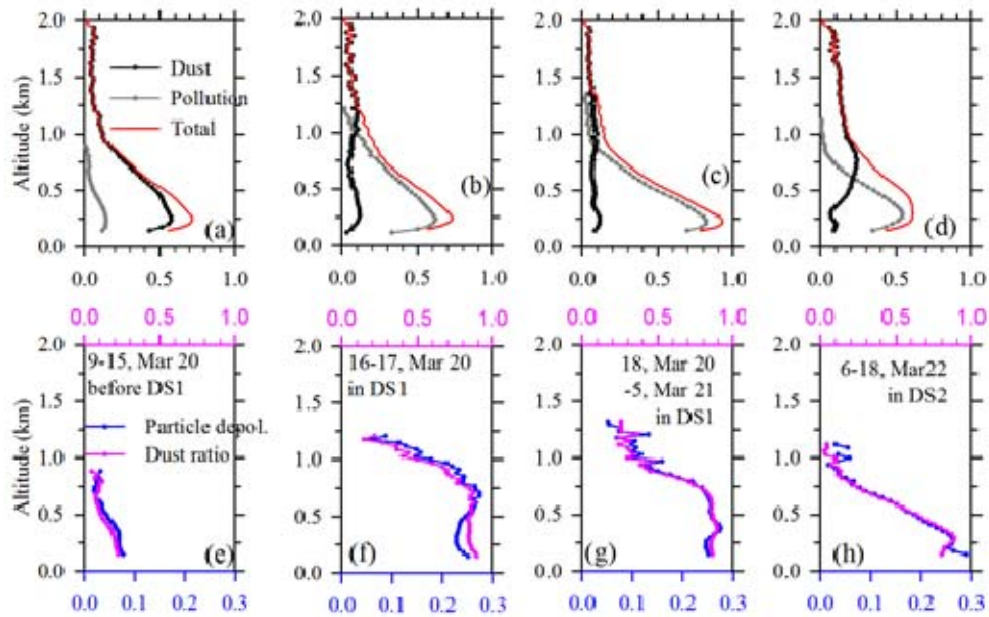
1107  
1108



1109  
1110  
1111  
1112  
1113  
1114  
1115  
1116  
1117  
1118  
1119  
1120  
1121  
1122  
1123  
1124  
1125  
1126  
1127  
1128  
1129  
1130  
1131  
1132  
1133

Fig.7 Variations of (a) the ratios of  $\text{Ca}^{2+}/\text{Ca}$ , (b) the equivalent concentrations of the total anions to the total cations (Anion/Cation), (c) the equivalent concentrations of  $\text{NH}_4^+$  to the sum of  $\text{SO}_4^{2-}$  and  $\text{NO}_3^-$  ( $[\text{NH}_4^+]/[\text{SO}_4^{2-}+\text{NO}_3^-]$ ), and (d) the equivalent concentrations of the sum of  $\text{NH}_4^+$ ,  $\text{Ca}^{2+}$ , and  $\text{Mg}^{2+}$  to the sum of  $\text{SO}_4^{2-}$  and  $\text{NO}_3^-$  ( $[\text{NH}_4^++\text{Ca}^{2+}+\text{Mg}^{2+}]/[\text{SO}_4^{2-}+\text{NO}_3^-]$ ) in TSP during March 19-22 and NDS, 2010.





1134  
 1135  
 1136  
 1137  
 1138  
 1139  
 1140  
 1141  
 1142  
 1143  
 1144  
 1145

Fig.8 Vertical profiles of the average extinction coefficients of dust, pollution, and total particles ( $\text{km}^{-1}$ ), particle depolarization ratios (Particle depol., unitless), and the ratio of the dust extinction in the total extinction (Dust ratio, unitless) in four periods of 9:00 - 15:00 of March 20 (before DS1), 16:00 - 17:45 of March 20 (before the highest  $\text{PM}_{10}$  concentration in DS1), 18:00 of March 20 - 4:45 of March 21 (during the highest  $\text{PM}_{10}$  concentration in DS1), and 6:00 - 18:00 of March 22 in DS2.

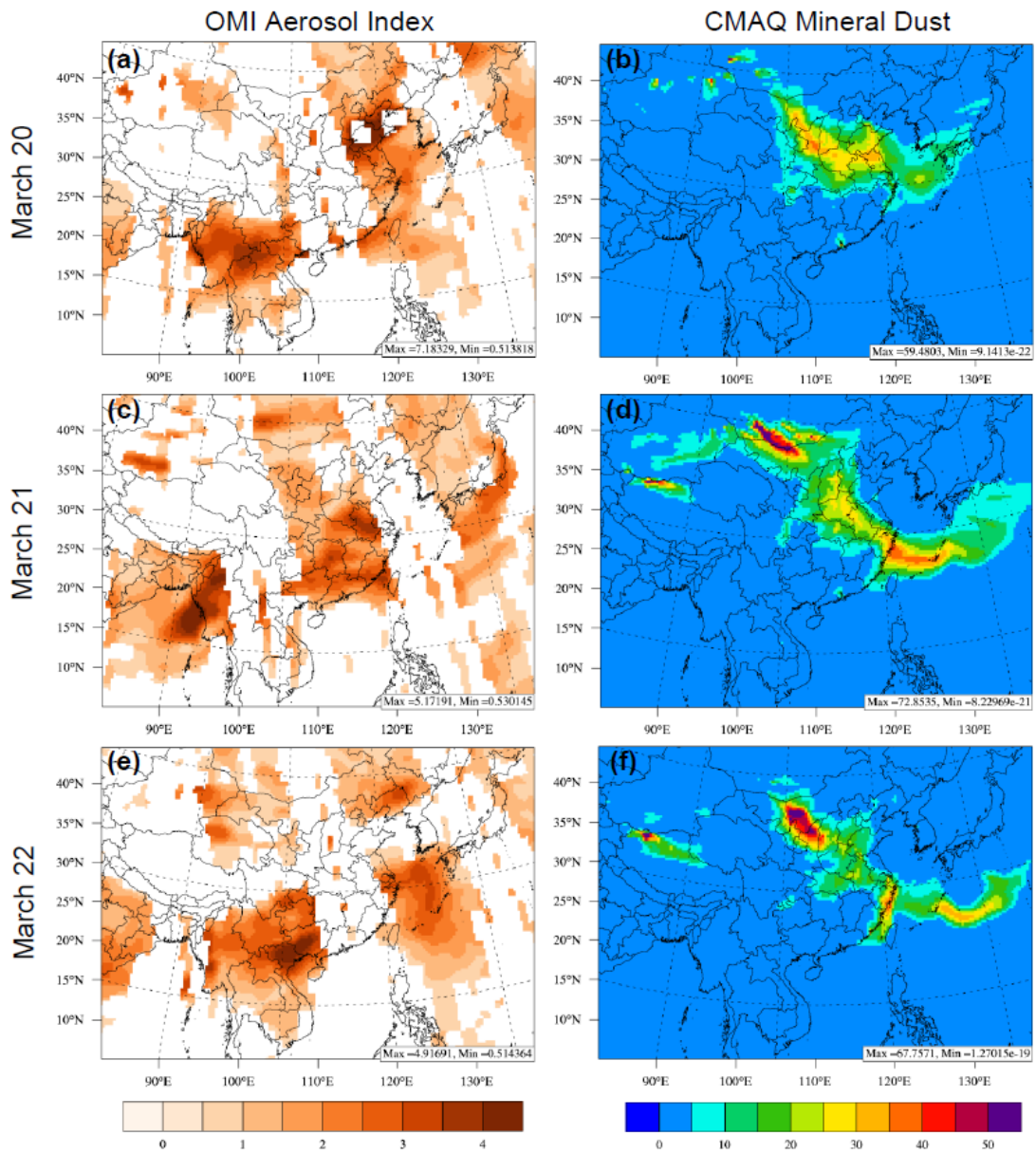


Fig. 9. The spatial distribution of OMI Ultraviolet Aerosol Index (unitless) and simulated mineral aerosols ( $\mu\text{gm}^{-3}$ ) from March 20 – 22, 2010, respectively.

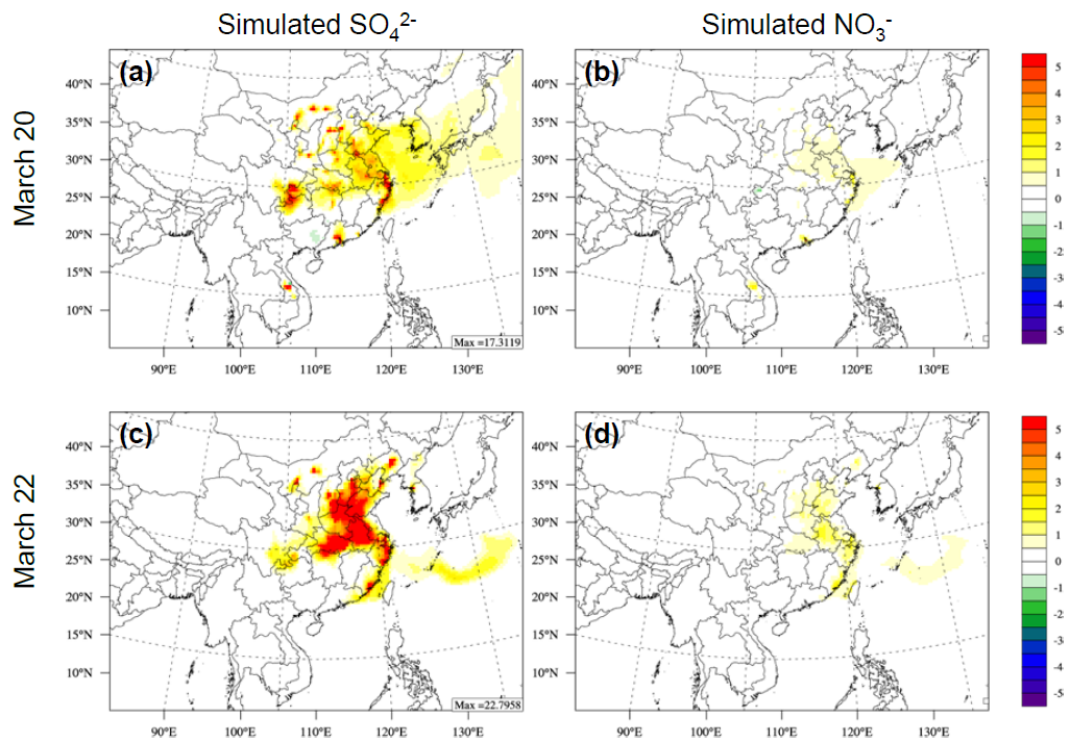


Fig. 10. Simulated  $\text{SO}_4^{2-}$  and  $\text{NO}_3^-$  ( $\mu\text{g m}^{-3}$ ) from dust heterogeneous reactions during DS1 and DS2.